CRUSTAL UNLOADING AS A SOURCE OF INDUCED SEISMICITY IN PLAINFIELD, CONNECTICUT

Sean M. Kondas

A thesis

submitted to the Faculty of

the department of Earth and Environmental Sciences

in partial fulfillment

of the requirements for the degree of

Master of Science.

Boston College
Morrissey College of Arts and Sciences
Graduate School

December 2020

CRUSTAL UNLOADING AS A SOURCE OF INDUCED SEISMICITY IN PLAINFIELD, CONNECTICUT

Sean M. Kondas

Advisor: John E. Ebel, Ph.D.

On January 12, 2015, a magnitude 3.1 mainshock occurred in Plainfield, Connecticut near Wauregan Tilcon Quarry, causing modified Mercalli II-IV intensities. Shortly after the event, a team from Weston Observatory installed portable seismographs in the epicentral area. The portable array detected hundreds of small earthquakes from around the quarry, with 26 events that were accurately located. P-wave first motion directions obtained from readings of the mainshock suggest a thrusting focal mechanism on a NNE-SSW trending fault. In this research, we collected 113 gravity measurements in the proximity of the quarry to verify and correct local fault geometry proposed by historic aeromagnetic and geologic mapping. Interpretations of the computed simple Bouguer anomaly are consistent with historic mapping, with a few exceptions. The gravity survey constrains a NNE-SSW trending fault that dips west underneath the quarry, inferred to be the Lake Char-Honey Hill Fault, and reduces ambiguity in the position of an undefined ESE-WNW trending fault, which appears to be on strike to intersect the quarry. A 3D boundary element program (3D~Def) is used to simulate quarry-induced stress changes on these faults in order to analyze the possibility of inducing seismicity through crustal unloading in the region. Quarry operations resulted in the removal of mass from the crust, which decreased lithostatic load. In a setting confined by a maximum horizontal compressional stress, decreasing the lithostatic load, or

minimum principal stress (σ_3), shifts a Mohr-Coulomb diagram toward failure. The boundary element model shows that following the excavation of materials at the quarry, positive Coulomb failure stress changes (ΔCFS) occur on the west dipping Lake Char-Honey Hill Fault. In agreement with past studies, our results suggest that quarrying operations can trigger seismic activity in specific settings with stress regime, fault orientations, and rock characteristics such as those that exist in the northeastern U.S. In order to mitigate the risk for future earthquakes related to quarrying operations, these factors must be considered before operations begin.

TABLE OF CONTENTS

LIST OF FIGURES

LIST OF TABLES

ACKNOWLEDGEMENTS

I would like to express my sincere gratitude to the faculty members of the Department of Earth and Environmental Sciences for their unconditional support and guidance over the course of my experience at Boston College. In particular, I want to thank Dr. John E. Ebel and Dr. Mark D. Behn for their invaluable scientific insights and rapid resolve regarding this project, despite the turbulent state of the contemporary world. Additionally, I am grateful to Thomas Vezmar, Achille Monod, and Dr. Margaret Thomas for their assistance in conducting the field surveys that were integral to this investigation. Finally, I am thankful for the rest of the staff at Weston Observatory who I was always able to look to for encouragement and positivity. Without the support of these great people, this research would not have been possible.

Introduction

Industrial activities can generate earthquakes of magnitude (M) > 4, which can cause millions of dollars of damage to infrastructure (Seeber et al., 1998). The largest events induced by human activities, e.g., the 1967 Koyna earthquake of M 6.3, can lead to loss of human life (Gupta, 2002). Many research efforts currently focus on earthquakes caused by fluid injection because of the recent surge in seismic activity surrounding wastewater injection in Oklahoma, Texas, and other areas (Weingarten et al., 2015). However, other physical processes, including fluid removal, hydraulic fracturing, and mass loading/unloading, must be considered for a complete understanding of the seismic hazards caused by industrial activity (Doglioni, 2018). Globally, more than 90 sites have been identified where earthquakes have been triggered by the filling of water reservoirs, i.e., mass loading (Gupta, 2002), while only a few sites have been identified in the published literature where earthquakes have been triggered by mass unloading through quarrying operations (Gibowitz, 1982; Seeber et al., 1998; Pomeroy et al., 1976).

The most recent investigation of seismicity induced by mass unloading in the northeastern U.S. was after a magnitude 4.6 earthquake occurred within the upper 2.5 km of the crust underneath a large quarry in Cacoosing Valley, Pennsylvania (Seeber et al., 1998). In the months following the mainshock, a swarm of aftershocks clustered around the periphery of a tabular 3 x 3 km zone that was interpreted to outline the mainshock rupture. Seeber et al. (1998) showed that the event occurred as the result of a thrusting mechanism with left-lateral slip, and that roughly $2 million of damage occurred in the surrounding area due to this earthquake, which at the time, was the highest amount of damage caused by an earthquake in the eastern United States since 1944. Since the Cacoosing valley event, the focus of induced seismicity research has largely shifted towards injection-induced seismicity following the development of unconventional hydrocarbon resource extraction in the mid 2000s. However, the continued improvement in our understanding of the relationship between quarrying operations and seismic activity is warranted. The relative lack of published examples of seismicity induced by crustal mass unloading suggests that a contribution to the investigation of this topic is overdue.

On January 12, 2015, a magnitude 3.1 earthquake centered about 500 meters east of the abandoned Wauregan Tilcon Quarry (also known as Wauregan Quarry) in Plainfield, Connecticut caused modified Mercalli II-IV intensity shaking to be felt in Connecticut, Rhode Island, and Massachusetts (Fig. 1). Shortly after the event, a team from Weston Observatory installed portable seismographs in the epicentral area. In agreement with past studies (Gibowitz, 1982; Seeber et al., 1998; Pomeroy et al., 1976), P-wave first motion directions obtained from the aftershock readings of the portable seismographs and surrounding networks suggest a thrusting focal mechanism. In the following months, the portable array detected hundreds of small earthquakes in the area immediately surrounding the quarry, with 26 events that were accurately located (Fig. 2). The focal depths of the accurately located events are less than 1.7 km, with many of the events having focal depths of less than 1 km (Ebel, 2016). The events were separated into three different time segments to emphasize the spatial development of the swarm with time. The first eight of these events took place roughly parallel to the north-south oriented, west-dipping Lake Char Fault (Fig. 2a), whereas many of the later events took place primarily on a WNW-oriented trend that is on strike with a mapped fault to the northwest (Fig. 2b-c).

Earthquakes in the northeastern U.S. occur in varying styles, ranging from single events that are isolated in time and location to swarms that can involve hundreds of microearthquakes and last for months within a small epicentral region. Although the Plainfield swarm began in January 2015, three small precursory events in fall 2014 were detected by regional seismic stations in southern New England. On 13 October 2014 an earthquake of M_{Lg} 0.9 was located in Plainfield. On 9 November 2014 two additional small earthquakes (M_{Lg} 0.6 and M_{Lg} 0.9) were located at approximately the October epicenter. The swarm was heralded on 8 January 2015 with an M_{Lg} 2.0 event that took place at 9:28 a.m. local time (Ebel, 2016). Following the mainshock on January 12 and subsequent installation of the portable seismic stations, more than 180 microearthquakes were confirmed based on the similarity of their waveshapes with larger events. Figure 3 shows a timeline of all swarm events of M -1.0 and greater. The method of Ebel et al. (2008) utilizes relative P and S arrival times computed using waveform cross-correlations to compute a highly accurate hypocenter of one event relative to that of another event. P and S waveforms from regional seismic network stations L63A, UCCT, BRYW, M63A, M62A, and HRV (listed here in order of increasing epicentral distance from 26 km to 84 km) were used to locate the mainshock epicenter with relative uncertainty of a few kilometers. The mainshock was computed to have a focal depth that was about 125 m ± 96 m shallower than that of Event 4 (Fig. 2a), suggesting that the mainshock took place very close to the surface of the earth. The quarry in question, which produced crushed stone for road production, was closed in 2011 and has been inactive since then. Recent surveys of the area show that the quarry has not filled with water since its closure.

In this research, we investigate the relationship between Wauregan Quarry and the seismicity that occurred in Plainfield in 2015. We conduct a gravity survey in the area surrounding the quarry to approximate fault orientations. The positions of the faults, in addition to parameters accounting for local stress regime and rock properties, are implemented in a deformation modeling program called 3D~Def (Gomberg and Ellis, 1994). This forward modeling approach is used to recreate local stress changes imposed on the upper crust as a result of the quarrying operations. My goal is to evaluate the possibility of whether the quarry activities induced the Plainfield earthquakes and elucidate whether future quarrying operations could lead to more earthquake activity in the area of the quarry.

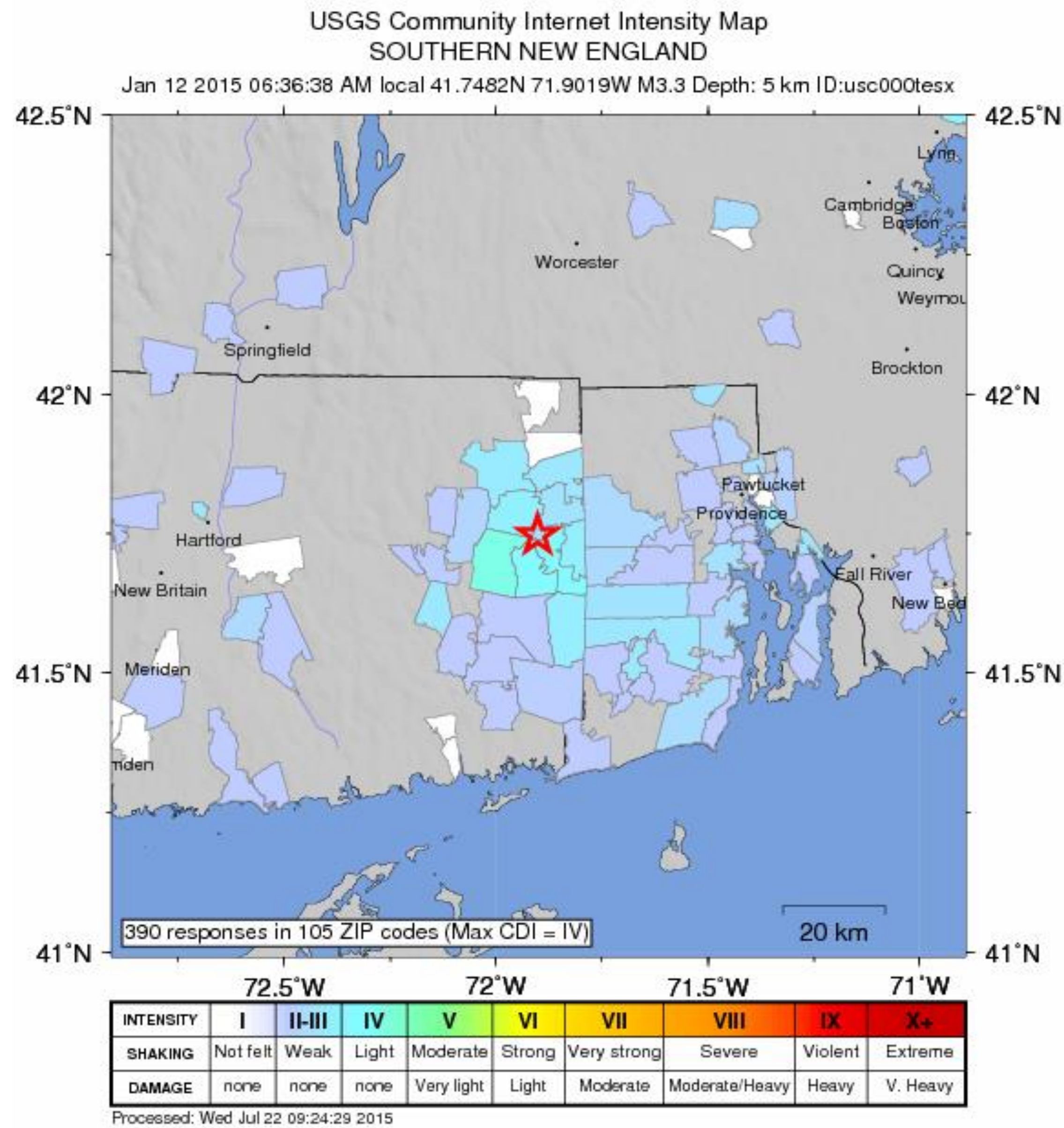

Fig. 1. Felt modified II-IV Mercalli shaking intensities seen throughout Connecticut, Rhode Island, and Massachusetts as a result of the 2015 magnitude 3.1 earthquake in Plainfield. Mainshock location represented by red star. From Ebel (2016).

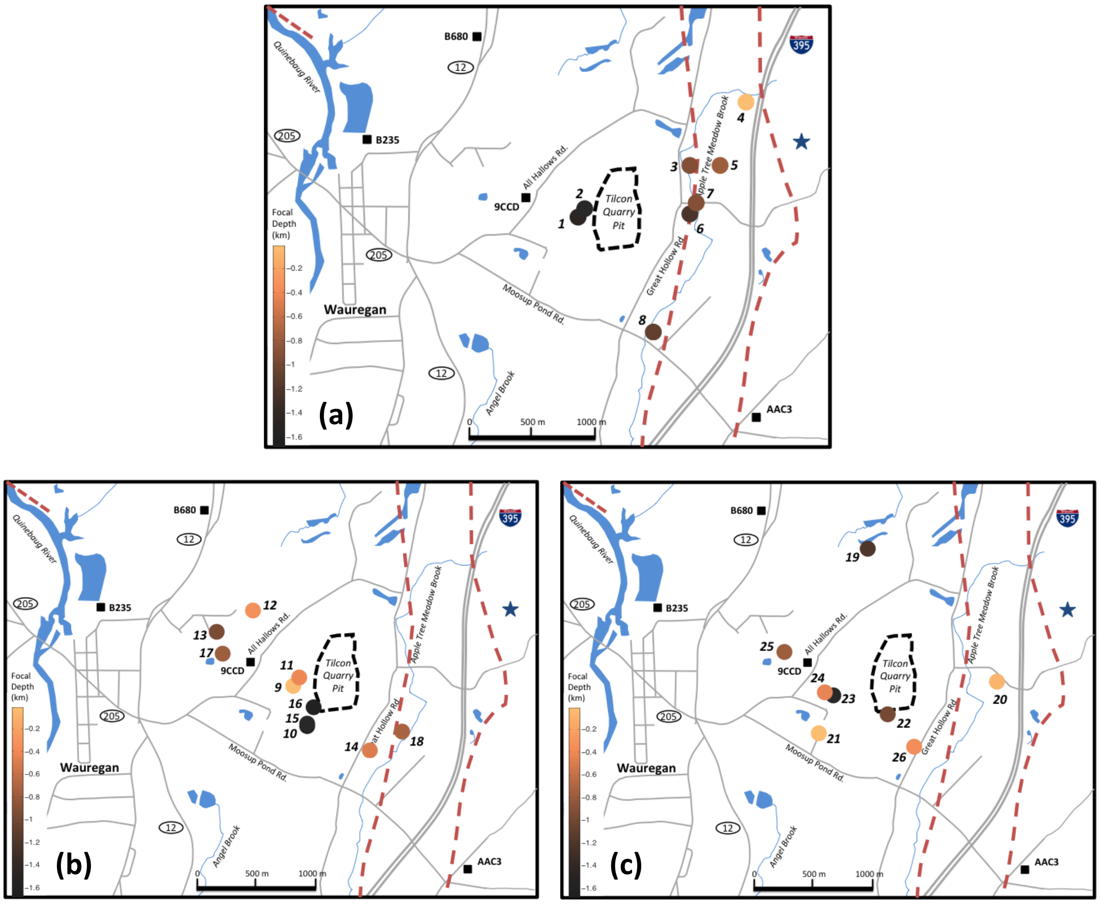

Fig. 2. Accurately located hypocenters of aftershocks following the M 3.1 mainshock (blue star) in Plainfield, CT in 2015. Circles represent hypocenter locations numbered chronologically as they occurred throughout the months following the mainshock. Spatiotemporal development is seen along the Lake Char Fault (a), along a southeast trending fault (b), and somewhat randomly distributed (c). Black squares represent installed portable seismograph stations. Quarry area outlined in dashed black line. Mapped faults outlined in dashed brown lines. From Ebel (2016).

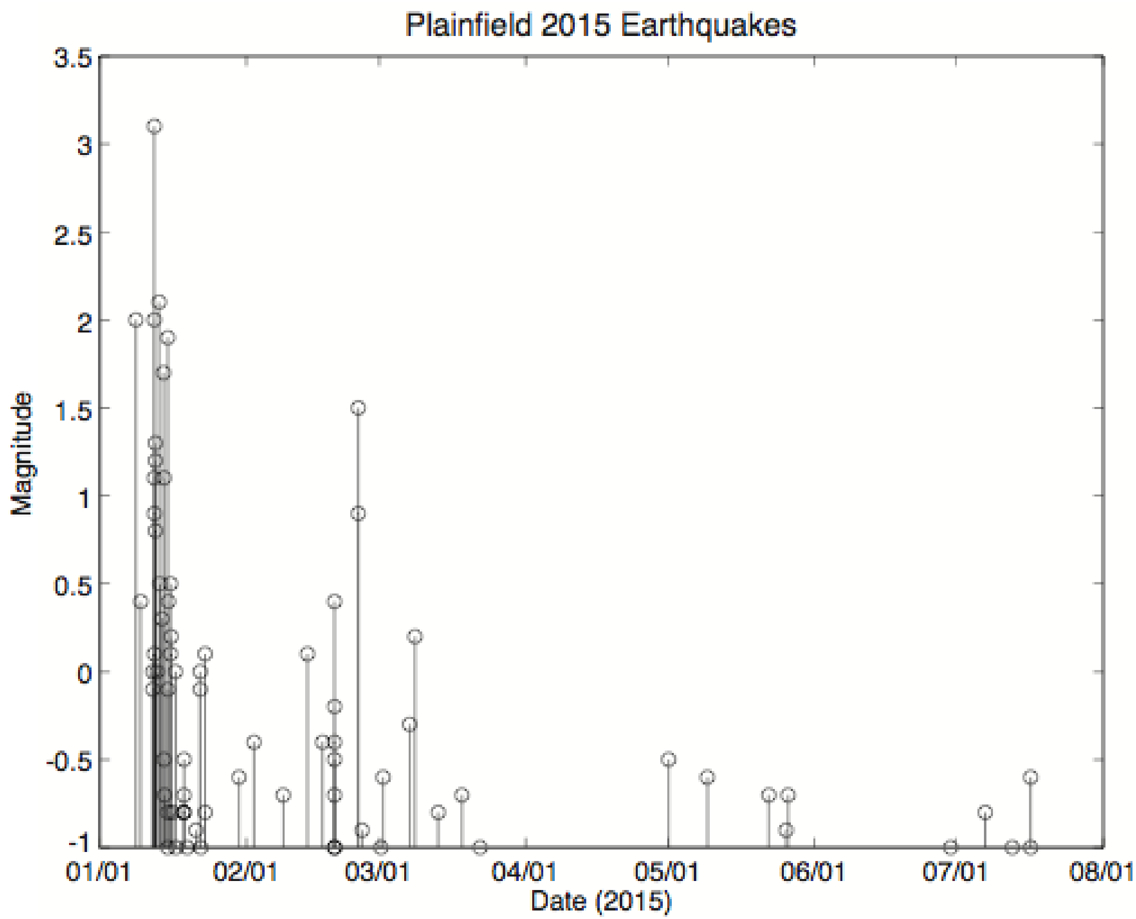

Fig. 3. Timeline of all swarm events of magnitude -1.0 and greater. Magnitudes computed using a linear regression of the maximum amplitudes of the events at portable station 9CCD with the computed magnitudes of the larger events from the regional seismic network. From Ebel (2016).

1.0 Background

1.1 Earthquake Activity in New England

The northeastern United States formed as the result of a series of orogenic events that occurred over the past ~1.1 billion years. Major tectonic events that contributed to the geological assembly of this region, including the Grenville, Taconic, and Acadian Orogenies are preserved in the subsurface. Since the rifting of Pangaea (180 m.a.), the region has been tectonically inactive and is considered a passive continental margin. However, the northeastern United States is one of the most seismically active areas east of the Rocky Mountains. The area has a long and continuous history of earthquake activity, and it has experienced strong, damaging earthquakes on various occasions. For example, the 1755 Cape Ann earthquake, which had a magnitude of about 6.0-6.2, did significant damage to manmade structures in Boston (Ebel, 2006). A recurrence of the 1755 earthquake would likely lead to several billion dollars of damage just within the city limits of Boston (1996 HAZUS study for the City of Boston).

Compared to most intraplate zones, the area within a 100 km radius of New York City has had an intermediate level of seismic activity throughout its recorded history (Kafka et. al, 1985). This region is clearly not as seismically active as parts of the Western United States, such as California; neither has this region experienced historic earthquakes as large as the 1811 to 1812 events located near New Madrid, Missouri (estimated $M > 7.2$). However, the greater New York City area, northern New Jersey, and Connecticut have had their share of moderate size earthquakes when compared to the rest of the northeastern United States. Boston College maintains a catalog with records of measured and observed earthquakes in the northeastern United States and southeastern

Canada from June 1638 to Jan. 2014. In the dataset, a dramatic increase in the number of recorded events occurs starting in the late 20th century. Around this time, public interest in the earth sciences was growing and large advances in geophysical technology were being made – most notably the implementation of a regional seismic network in the 1970s. Consequently, earthquake data from before the late 20th century is less comprehensive. However, notable patterns in the spatial distribution of these events are discernable and significant for the purposes of this study.

In Connecticut, the spatial distribution of recorded seismic events is not uniform. Over the last almost 400 years, it appears that the highest concentration of seismic events in the state occurred around the town of Moodus in a SSW-NNE trending region roughly parallel to the fault zone separating the Merrimack Synclinorium and the Bronson Hill terrane, around 40 km southeast of Hartford. These events coincided with swarms of hundreds of microearthquakes and occurred from 1980-1989, with a maximum coda magnitude M_c of 2.9 and depths of less than 2.4 km (Ebel, 1989). A second area of relatively highly concentrated seismic activity is located about 45-km SSW of the epicenter of the 2015 Plainfield mainshock in southeastern Connecticut, along the east-west oriented Honey Hill segment of the Lake Char-Honey Hill map trace (Fig. 4). Prior to the onset of the earthquake swarm that is the subject of this research, no seismic activity had been recorded in a radius surrounding Plainfield for over 20 km.

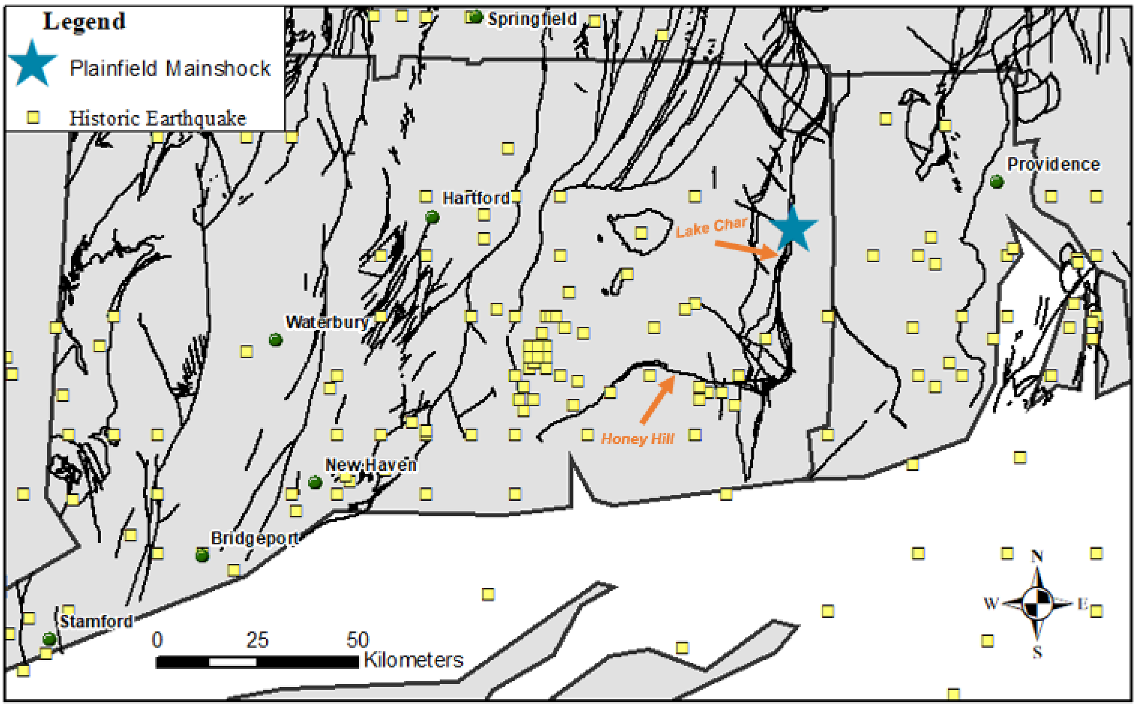

Fig. 4. Map of measured and observed recorded earthquake epicenters in the area around Rhode Island and Connecticut 1638-2014. Areas of increased event density are evident in southcentral and southeastern Connecticut. Location of M 3.1 mainshock that occurred in Plainfield in 2015 represented as blue star. Segments of Lake Char-Honey Hill Fault are distinguished. Known faults in the region are displayed.

1.2 Regional Structure

The Tilcon Wauregan Quarry lies completely within the Quinnebaug Formation, which is a thrust fault bounded green ophiolitic metaigneous island arc rock, accreted onto the North American continent during Devonian time in the Acadian Orogeny (Rodgers, 1985; Dixon, 1965). Historic mapping shows a complex of geologic structures with vertical and southward plunging folds (Dixon, 1965; 1968), although most of the structural field data from the quarry no longer exist due to the rock excavation. The formation is just to the west of a variably 600-m wide Paleozoic mylonite zone of rock, which marks the Lake Char segment of the Lake Char-Honey Hill Fault. Lake Char-Honey Hill refers to a curved map trace composed of the north-south trending Lake Char and the east-west trending Honey Hill Fault (Fig. 4), which is a major geologic suture that marks the tectonic closure of the proto-Atlantic (Wilson, 1966), or Iapetus Ocean. The north-south and east-west trending fault segments meet and conjoin around a sharp 90° bend north of Ledyard, Connecticut. Microstructural analysis of foliations and lineations in the mylonitic rocks around the fault bend suggest syn- or post- faulting tightening of the bend, as well as accommodation of slip along a curved, spoon-shaped surface (Growdon et al., 2005).

Historic mapping from Dixon (1965; 1968) shows structural measurements from outcrops that existed before the quarry was developed. Inferred high angle faults mapped by magnetics were identified within the Quinnebaug formation to the west of the quarry, striking 23° and 24° (Thomas, 2019). These are truncated by two near parallel faults trending southeast 120° and 123°. The northern of these two faults is ~1.8 km north from the center of the quarry, and its southern equivalent appears to be on trend to intersect the southwestern corner of the quarry had it been mapped in the Plainfield quadrangle (Fig. 5). Following the Plainfield mainshock, a portable seismic array deployed from Weston Observatory was used to accurately locate aftershock hypocenters that appear to be on strike with this fault (Fig. 2b). Although Dixon mapped the bedrock geology of both the Danielson and Plainfield quadrangles, the separation in time between the publishing dates of each map might account for the abrupt discontinuity seen in the plotted extent of the southern southeast trending fault at the quadrangle boundary. For this study, we conducted gravity and magnetic surveys in the area in order to reduce uncertainty in the geologic structure and to further constrain the extent of the southeast trending fault in question (Fig. 5).

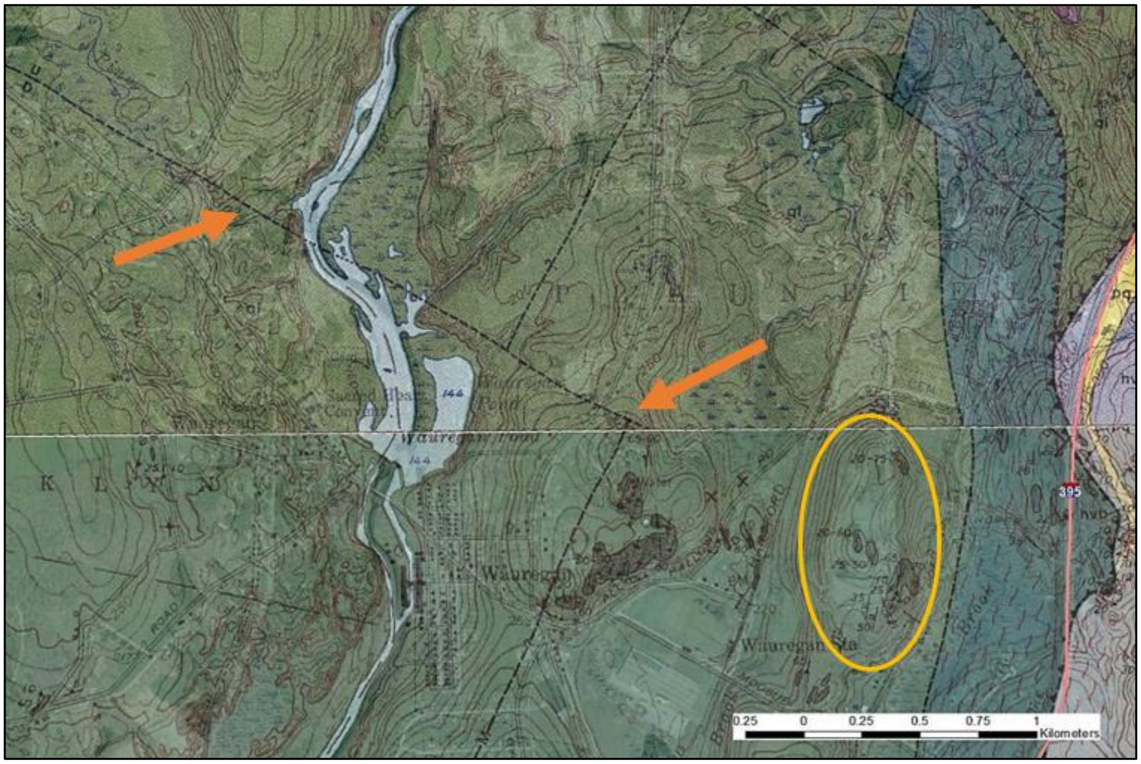

Fig. 5. Regional view of Historic Bedrock Mapping in the Wauregan Area (Dixon, 1965; 1968). Quinnebaug Formation in green; mylonitic rock in blue; Avalonian continental rocks in purple; quartzite in yellow. Quarry area marked by orange oval. Faults are noted with black lines; Lake Char Fault shown with teeth on upper plate. Southeast trending fault (marked by orange arrows) appears to be on trend to intersect the quarry. Horizontal white line marks the 7.5-minute quadrangle boundary between Plainfield to the south and Danielson to the north. Modified from Thomas (2019).

1.3 Fault Reactivation through Crustal Unloading

When an earthquake occurs, rock fractures and/or slip occurs on one or more preexisting fault planes. Defining principal stresses in the earth is a useful way to investigate the physical mechanisms that lead to brittle deformation in the upper crust (Anderson, 1951). Because the Earth's surface marks the transition from solid rock to a fluid, which cannot support shear tractions, it is a principal stress plane. Thus, one of the principal stresses (denoted σ_1, σ_2, or σ_3) will generally be normal to Earth's surface and can be described as the vertical stress (S_v). This assumption can be held as true to around 15-20 km depth where the brittle-ductile transition zone begins (Zoback, 2007). In a normal faulting regime, S_v is the maximum principal stress (σ_1), the maximum horizontal stress (S_{Hmax}) is the intermediate principal stress (σ_2), and the minimum horizontal stress (S_{hmin}) is the minimum principal stress (σ_3). In a reverse faulting regime, S_{Hmax} is the maximum principal stress, S_{hmin} is the intermediate principal stress, and S_v is the minimum principal stress (Fig. 6). Stable continental regions are commonly at near-critical stress conditions, such that small mechanical changes can alter principal stress magnitudes and trigger earthquakes (Simpson, 1986). Ostensibly, corporations that plan to conduct industrial activities like quarrying (mass removal) and water reservoir construction (mass loading), which can significantly affect principal stresses, must consider the regional stress regime before operations begin, so that the potential for seismic hazard can be limited.

In order to generate seismic activity induced by crustal unloading, mass removal must occur in a contractional tectonic region – a reverse faulting regime – with a preexisting critical state of stress (Simpson, 1986). As the lithostatic load is reduced in

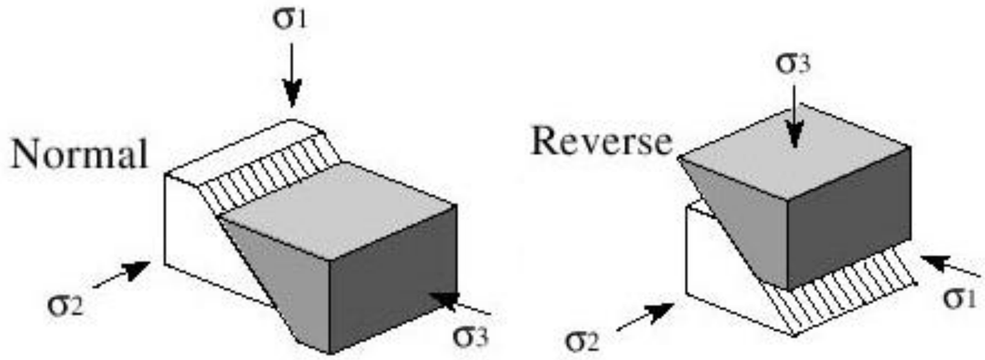

Fig. 6. Principal stress orientations for normal (left) and reverse (right) faulting regimes. Normal regimes show dominant vertical stress whereas reverse regimes show dominant horizontal stress. From *www.geosci.usyd.edu.au*.

this setting, the differential stress ($\sigma_1 - \sigma_3$) between the vertical stress (σ_3) and the maximum horizontal stress (σ_1) becomes sufficiently large such that the frictional strength of the rock can no longer support the shear stress (Fig. 7; Scholz, 2002). The minimum horizontal stress (σ_2) does not need to be considered in order to determine this failure criterion (Simpson, 1986). Horizontal components of stress are complex and largely subject to tectonic variability around the globe. However, it is relatively straightforward to determine the vertical stress using the following equation:

$$S_v = \int_0^Z \rho(Z) g \, dZ \tag{1}$$

where Z is depth from the surface, g is acceleration from Earth's gravity, and ρ is density of the rock as it changes with depth (Zoback, 2007). Industrial activities can alter the magnitude of S_v by adding or removing mass from the upper crust. When mass is removed, S_v is reduced, and in a reverse faulting regime, the differential stress increases toward failure.

The relationship between the differential stress and the frictional strength of the rock can be demonstrated on a Mohr diagram (Fig. 7). The Mohr-Coulomb fracture criterion represents the failure envelope on the diagram and is given by the equation:

$$\tau = \tau_0 + \mu\sigma_n \tag{2}$$

where τ is shear stress, τ_0 is a cohesion term, μ is the coefficient of internal friction, and σ_n is the stress normal to the fault plane (Scholz, 2002). The Mohr diagram shows that rock at its failure point is described by the stress states that "touch" the failure envelope. Stress states that do not intersect the failure envelope imply that rock will not be fractured. We can express the normal stress σ_n and shear stress τ in Eq. 2 in terms of σ_1 and σ_3 with the following equations:

$$\tau = 0.5(\sigma_1 - \sigma_3)\sin 2\theta \tag{3}$$

$$\sigma_n = 0.5(\sigma_1 + \sigma_3) - 0.5(\sigma_1 - \sigma_3)\cos 2\theta \tag{4}$$

where θ is the angle between the fault normal and σ_1. Additionally, the equations show how differential stress between maximum and minimum principal stresses affects the terms in the fracture criterion. However, the Mohr-Coulomb fracture criterion applies to idealized conditions involving unfractured rock. Assuming the 2015 seismic events in Plainfield occurred because of crustal unloading; we consider the reactivation of preexisting faults proximal to the quarry, which cannot be fully described by the Mohr fracture criterion for unfractured rock, but rather by a friction criterion for slip on a fault.

The frictional strength of faults is less than the stress necessary to form them; once formed, they constitute planes of weakness that may be reactivated in stress fields that are not optimally oriented (Scholz, 2002). The stress condition for reactivating a fault inclined at an angle θ to σ_1 is:

$$\frac{(\sigma_1 - P_p)}{(\sigma_3 - P_p)} = \frac{(1 + \mu \cot\theta)}{(1 - \mu \tan\theta)} \tag{5}$$

where P_p is pore pressure and μ is the coefficient of internal friction (Sibson, 1985). Given a fault at the optimal angle $\theta = \beta$ for frictional sliding, the friction criterion for failure is less than the Mohr-Coulomb fracture criterion for the same unfractured rock type. If a fault is at the optimal angle β for frictional sliding, that is, critically oriented, we can say (Zoback, 2007):

$$\beta = \frac{\pi}{2} - \tan^{-1}\mu \tag{6}$$

Assuming $\mu \approx 0.6$, a frictional coefficient commonly found in granitic rocks, the equation suggests that reverse faults optimally dip with $\beta \approx 30^\circ$ and strike normal to the direction of S_{Hmax}. If we also assume hydrostatic pore pressure, Equation 5 suggests a frictional limit of $\frac{\sigma_1}{\sigma_3} \approx 3.1$ for a critically oriented reverse fault (Sibson, 1985). In a reverse faulting regime, after determining the amount of mass removed and solving for the minimum principal stress S_v, the maximum principal stress S_{Hmax} can be theoretically estimated using the frictional limit.

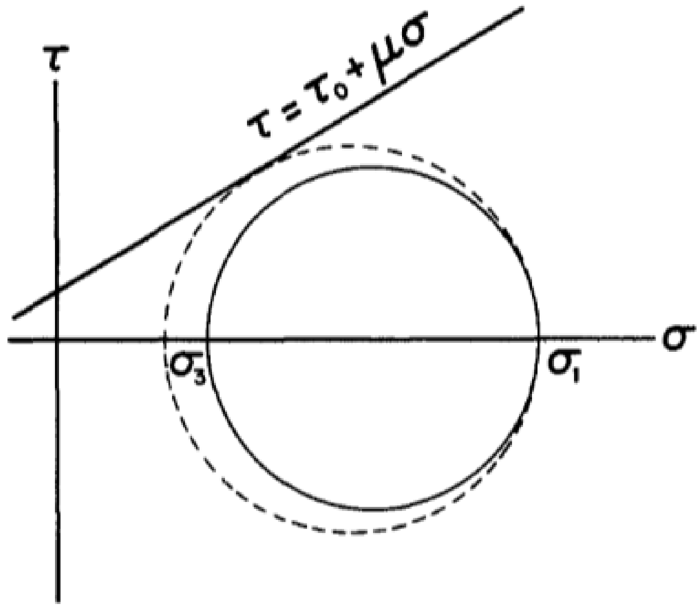

Fig. 7. The Mohr diagram and Mohr-Coulomb fracture criterion show the relationship between failure planes and stresses in the earth. As σ_3, the lithostatic load in a contractional setting, is lowered, the radius of the circle increases, driving the system toward failure. σ_1 is the maximum principal stress and σ_3 is the minimum principal stress. From Pomeroy et al. (1976).

1.4 Stress Regime in New England

Multiple studies have indicated a generally E-W to NE-SW oriented S_{Hmax} throughout the northeastern United States (Hurd and Zoback, 2012; Sykes and Sbar, 1973; Zoback and Zoback, 1991; Ebel and Kafka, 1991) in agreement with a wide variety of stress indicators that can be seen on the Karlsruhe Institute of Technology World Stress Map (WSM) database (Heidbach et al., 2016). Hurd and Zoback (2012) compiled stress data including 75 earthquake focal plane mechanisms and 10 formal stress inversions from the central and eastern United States and southeastern Canada (Hurd and

Zoback, 2012). Using this data, they calculated the AΦ parameter, which ranges from 0 (uniform horizontal extension with $S_v >> S_{Hmax} = S_{hmin}$) to 1.5 (strike-slip faulting with $S_{Hmax} > S_{hmin} > S_v$) to 3 (uniform horizontal compression with $S_{Hmax} = S_{hmin} > S_v$) to map faulting styles and relative stress magnitudes across the region. The study indicates a highly consistent, compressional, NE-SW oriented maximum horizontal stress across much of intraplate North America (Fig. 8). The paper found a clear transition from predominantly strike-slip faulting in the south-central U.S. to predominantly thrust faulting in the northeastern U.S. and southeastern Canada, which reflects increasing compressive horizontal stresses with respect to the vertical stress from central to northeast North America.

Using a set of 46 focal plane mechanisms from the northeast United States and parts of southeastern Canada, Ebel and Kafka (1991) determined an average P axis trend of 86˚ ± 40˚. Roughly 70 km from the study area in Plainfield, well bore breakout analysis in Moodus, CT suggest a regional S_{Hmax} azimuth of 89˚ (Moos and Zoback, 1990). Stress orientations are uniform with depth, independent of lithology and age (Zoback, 2007). Additionally, intraplate stresses predominantly vary as a function of large-scale tectonic processes (Sykes and Sbar, 1973). Thus, in this investigation of the 2015 earthquakes that occurred in Plainfield, we make the assumption that S_{Hmax} is oriented E-W.

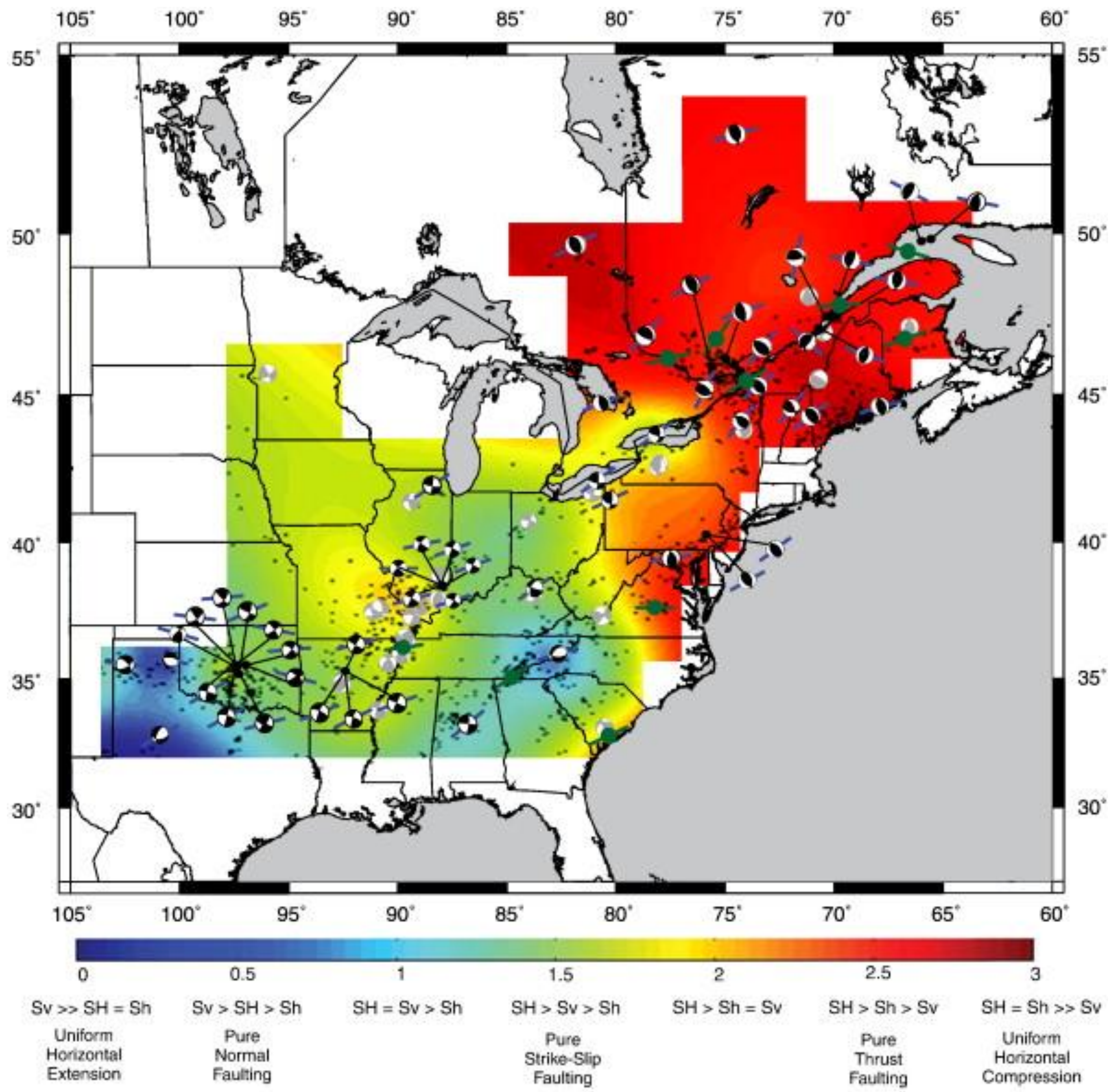

Fig. 8. Spatial variation in regional stress state as defined by the AΦ parameter. Horizontal stresses become increasingly compressive (AΦ becomes larger in value) with respect to the vertical stress moving from the south-central U.S. to the northeastern U.S. and southeastern Canada. Values are interpolated using a bilinear interpolation scheme, and extrapolated linearly to the boundaries of the map. Background seismicity is from the USGS/NEIC catalog 1973–2010 [published caption]. From Hurd and Zoback (2012).

2.0 Methodology

2.1 Introduction

In August 2019, I conducted gravity and magnetic surveys around Wauregan Quarry with the assistance of two student interns (Achille Monod and Thomas Vezmar, University of Strasbourg, FR). The primary objective of the geophysical survey is to reduce ambiguity in subsurface structure left behind by historic geologic mapping. As described in section 1.2, the division between the northern Danielson quadrangle and southern Plainfield quadrangle coincides with the mapped termination of a southeast trending fault, which appears to be on strike to intersect the southwestern corner of the quarry had it been mapped in the Plainfield quadrangle (Fig. 5). In addition to contributing to a better understanding of the tectonic stress regime in the region, better constraints on the geometry of this fault allow for more representative modeling of the scenario that led to the 2015 Plainfield earthquakes.

The most recent aeromagnetic and gravity surveys of our study area were conducted throughout the mid to late 20th century and their results are available at relatively low resolutions. In order to improve the resolution of geophysical data in the study area, we first attempted to carry out ground-based magnetic surveys across mapped faults in the region. We took proton-precession magnetometer measurements with ~25 meter spacing across two faults, including a southeast trending fault north of the quarry and the southeast trending fault in question, which are both indicated on the bedrock geology map of the Danielson Quadrangle (Dixon, 1968), and found evidence to support their mapped positions. However, the area largely consists of densely populated suburbs and private property, which unfortunately complicated magnetometer data collection and ultimately influenced the decision to abandon the ground-based magnetic survey. Instead, we use historic aeromagnetic data from the USGS (Zietz et al., 1974; Fig. 9), in addition to the data obtained from our gravity survey to approximate the subsurface structure.

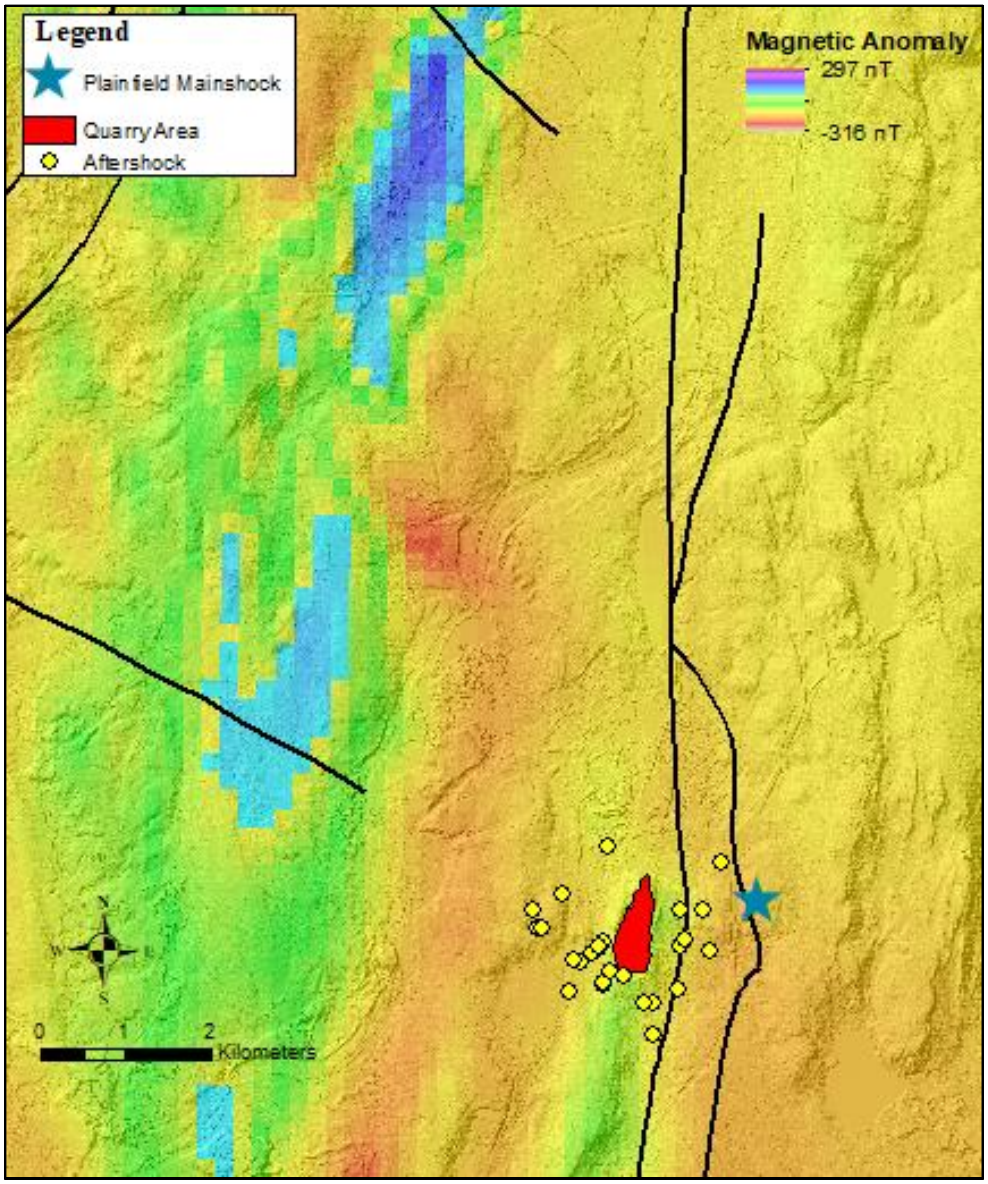

Fig. 9. Historic aeromagnetic map (Zietz et al,. 1974) over hillshade map of the area surrounding the Wauregan Quarry in Plainfield, CT. Black lines represent mapped faults.

The aeromagnetic data is used to differentiate the magnetic content of rock formations by measuring the scalar intensity of the local total magnetic field surrounding Wauregan Quarry. The anomalous response from the local geology can be determined after subtracting the undisturbed main field from the total field reading. The following equation demonstrates how this is possible:

$$(F_E + F_{A_T})^2 = (Z_E + Z_A)^2 + (H_E + H_A)^2 \tag{7}$$

where F_E is the total response from the undisturbed main field, F_{A_T} is the total anomalous response parallel to the main field, Z_E and H_E are the vertical and horizontal components of the undisturbed main field, and Z_A and H_A are the vertical and horizontal components of the anomalous response from the geology (Burger et al., 2006). Anomalies seen in aeromagnetic data suggest a change in the ferrimagnetic content of the geology and could signify the presence of subsurface structures like faults (Yan et al., 2018).

2.2 Gravimetry

We conducted a gravity survey over a roughly 60 km^2 area around the quarry in order to investigate the subsurface structure near the site of the 2015 Plainfield earthquake swarm. A total of 113 measurements were recorded with ~600 meter spacing along public roads. Gravity anomalies on this scale are the result of variation in density close to the Earth's surface. In many cases, a measured gravity anomaly involves juxtapositions of rocks of known type, so interpretation depends upon some knowledge of the average densities of rocks (Garland, 1979). Geologic interpretations from the bedrock mapping of the Danielson and Plainfield Quadrangles (Dixon 1965; 1968) serve to inform the rock density estimates.

Relative gravity measurements were obtained with a LaCoste & Romberg Model G-1189 with an Aliod100 upgrade. The system has a range of ± 50 mGal with a resolution of 0.01 mGal. The Leica GNSS GS14 RTK Rover was used to determine precise GPS points for measurements with 1-5 cm accuracy in elevation. Base station recordings were taken every two hours to account for instrumental drift and diurnal variation associated with sun and moon tides. In addition to correcting for variations seen at the base station, the latitude correction, the free-air correction, and the Bouguer correction were applied to the data. The simple Bouguer anomaly is obtained after applying the following corrections to the data, summarized by the equation:

$$\Delta g_B = \Delta g_{obs} + C_\varphi + C_F - C_B \tag{8}$$

where Δg_B is the relative Bouguer anomaly, Δg_{obs} is the relative observed value after subtracting base station variation, C_φ is the latitude correction, C_F is the free-air correction, and C_B is the Bouguer correction (Burger et al., 2006). The resulting simple Bouguer anomaly approximates the terrain as an infinite flat plate. A terrain correction was not applied to the data since the variation in elevation is inferred to be small enough to have an insignificant effect on the measured gravity (Nowell, 1999).

The survey was conducted in a loop manner whereby the day started with a gravity reading at the temporary base station, followed by a number of station readings and a return to that base station in two-hour intervals. Relative gravimetry requires that a location is set as the zero mGal reference point, such that deviations from that point define the relative changes in the local gravity field. In order to set the LaCoste & Romberg Model G-1189 to zero mGal, we used a counter value of 3827.4; this value varies with latitude and corresponds to the absolute observed gravity value. Measures of absolute observed gravity can be determined from the International Gravity Standardization Net (IGSN71), which would allow the results of this survey to be tied into absolute gravity values. A patch of concrete near the entrance to Wauregan Quarry served as the zeroed location on the gravimeter, around which value relative measurements were recorded. For each station reading, the instrument was set up on the hardest available ground surface and given 4 - 6 minutes to settle on a value, which was recorded manually in a journal. The raw data were entered into a spreadsheet whereby the corrections were applied to the data with MATLAB.

In order to correct for base station drift, a linear drift rate between base station readings was assumed. The fluctuation of gravity values due to tidal effects is subject to diurnal variation and can have a rate of change as high as 0.05 mGal/hour. By recording base station readings every two hours, the drift rate was accounted for by a linear approximation (Burger et al., 2006). Instrument drift, which is caused by small changes in the physical constants of gravimeter components, was also accounted for by a linear drift rate assumption. Two locations were used for the base stations: the first location was at the zero location near the entrance to Wauregan Quarry, and the second was about 6 km to the northwest near an abandoned construction site (Fig. 10). We recorded seven base station measurements at both the first and second locations. The drift rate (r) was established by dividing the difference in the initial and subsequent base values by the elapsed time between the base station readings. Gravity values corrected for drift and tidal effects (Δg_{obs}) are determined with the following equation:

$$\Delta g_{obs} = g_{raw} - [r(t - t_0) + (b - b_0)] \tag{9}$$

where g_{raw} is the manually recorded raw gravity value, t is elapsed time from the beginning of the survey to the recording of the current gravity station, t_0 is elapsed time from the beginning of the survey to the recording of the prior base station, b is the raw gravity value of the prior base station, and b_0 is the value to which the base stations will be corrected. The value of b_0 varies for differing base station locations; b_0 values are tied such that they represent the same alignment in the diurnal tidal cycle.

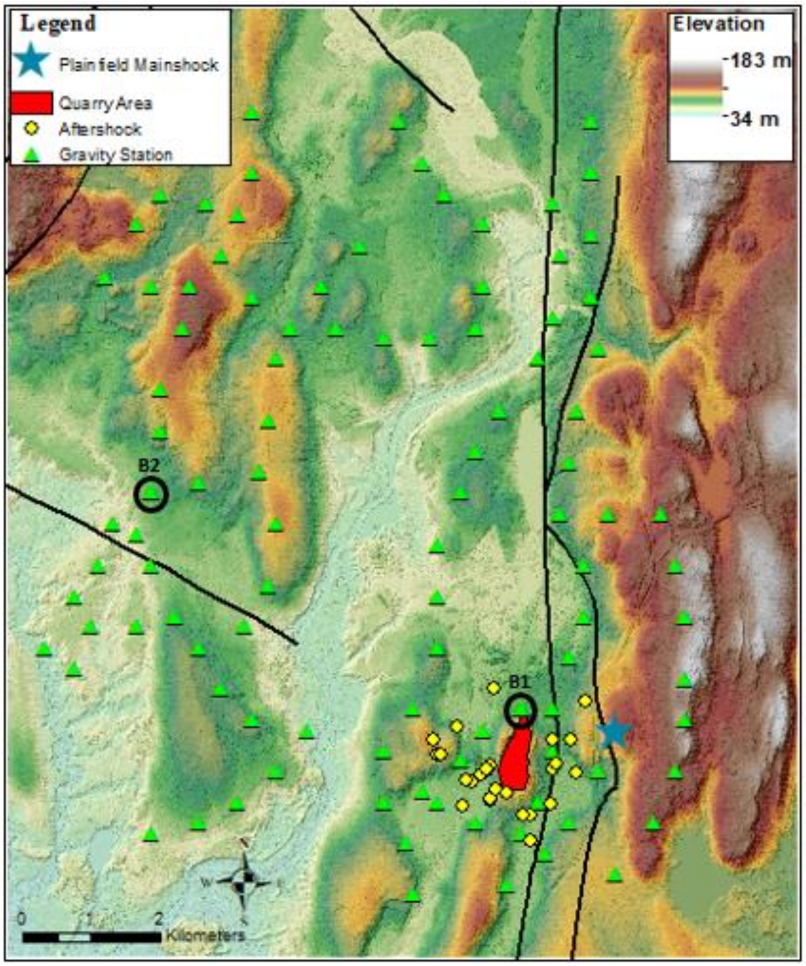

Fig. 10. DEM over hillshade map showing the extent of the gravity survey surrounding the Wauregan Quarry in Plainfield, CT. Black lines represent mapped faults. Black circles highlight base station locations; B1 is the first base station location, B2 is the second base station location.

Due to the centrifugal force produced by its rotation, the length of the Earth's radius is greater at the equator than at the poles. In addition to the effects caused by greater distance between the surface of the Earth and its center, the centrifugal force itself diminishes the measured value of gravity as the equator is approached (Burger et al., 2006). The latitude correction is applied to remove position on the Earth's surface as a cause of gravity difference. By taking the derivative of the geodetic reference system formula of 1967 with respect to latitude and converting to meters, we arrive at an equation that allows us to correct gravity values with respect to a chosen reference station. This correction is given by the following:

$$C_{\varphi} = -0.000812y * \sin(2c) \tag{10}$$

where y is the distance in meters between the reference station and the current station using the y-component of UTM coordinates; c is the reference station latitude in radians. Station coordinates are accurately determined with the Leica GNSS GS14 RTK Rover. Our chosen reference station uses the coordinates of the first base station near the entrance of Wauregan Quarry. Distances north of the reference station are positive and distances south of the reference station are negative.

The acceleration due to gravity (g) between two objects is proportional to the distance between them squared. Thus, it follows that the g imparted by the Earth on the position of a gravity station varies with elevation. The dependence on elevation is removed from gravimetry data by applying the free-air correction. By taking the derivative of the equation for gravitational acceleration, we can determine the gravitational vertical gradient. Assuming 45° latitude, the free air correction is given by the following equation:

$$C_F = 0.3086h \tag{11}$$

where h is orthometric height for a given station. Each station was corrected to a datum set at sea level. For the purposes of this study, orthometric height is synonymous with height above sea level and is determined for each station with the Leica GNSS GS14 RTK Rover. The Leica RTK Rover is capable of 1-5 cm accuracy in elevation, but for roughly half of the collected data points, connection to the local RTK network *(acorn.uconn.edu)* failed. Inability to connect to the RTK network resulted in recorded elevations with uncertainties of ± 6 m. Highly accurate elevation data is necessary for the free-air correction, so in order to correct the elevations we linked the gravity station coordinates to coordinates on 1-meter resolution LiDAR data obtained through the USGS. This solution is discussed further in the results (Section 3.1). The LiDAR data used to correct the elevations was used to generate the DEMs and hillshade maps seen in many of the figures of this study.

The free-air correction accounts for one of two elevation corrections necessary to compute the simple Bouguer anomaly. The second elevation correction, the Bouguer correction, is supposed to remove the effect of the additional mass above the datum that adds to observed gravity (Burger et al., 2006). This can be done by first deriving a relationship for gravity due to a very thin rod. The relationship derived for the rod is then integrated to compute the individual contributions to gravity from an infinite number of thin rods, making a sheet. Integrating again for an infinite number of sheets gives g due to a slab of infinite extent and thickness h. The resulting equation thus describes the Bouguer correction:

$$C_B = 0.04191\rho h \tag{12}$$

where ρ is assumed density of the infinite slab. An average crustal density of 2.67 g/cm^3 is assumed for the region surrounding the Wauregan Quarry and is used as the value of ρ in the computation of the Bouguer correction for all stations. Because this correction is supposed to remove the effect of mass above the datum that adds to Δg_{obs}, the correction is subtracted.

2.3 Modeling Crustal Unloading

A forward modeling approach is used to calculate the change in Coulomb failure stress due to the removal of rock at Wauregan Quarry. The three-dimensional boundary element program called 3D~Def is used to replicate the conditions that may have led to the earthquake swarm in Plainfield. 3D~Def uses Green's functions calculated using subroutines provided by Y. Okada. The Green's functions relate the deformation field to a rectangular dislocation in a homogeneous half-space. Dislocations are solved for to minimize strain energy in the medium, while satisfying stress boundary conditions on each dislocation surface (Gomberg and Ellis, 1994). We simulate a reduction in lithostatic load in the contractional setting of Plainfield with three boundary elements, or planar dislocations. Boundary elements are generally used to represent fault surfaces with 3D~Def applications, but in this model one of the three elements is implemented to apply the unloading stress associated with Wauregan Quarry, while the other two elements represent fault planes. Boundary conditions are applied to the central points of elements in the model input and may be specified in terms of relative displacement, shear or normal stress, and absolute displacement. The calculated reduction in vertical stress is applied as a negative normal stress to the quarry area, which is represented by a horizontally oriented element composed of 16 sub-elements.

In order to represent the stress changes imposed upon the Plainfield subsurface following the termination of quarrying operations, fault geometry, far-field stresses, rock strength parameters and the magnitude of the unload are determined. Data resulting from geophysical surveys, bedrock geology mapping, aftershock geometry and as reported in selected articles (Wilson, 1967; Thomas, 2019) are used to determine input fault geometry (Table 1). The maximum principal stress, σ_1, is assumed to be horizontal and oriented with 90° strike (Ebel and Kafka, 1991), perpendicular to the strike of the west dipping Lake Char Fault. Such geometry allows for the simplification of the Coulomb failure stress calculation in three dimensions (King et al., 1994), while maintaining a reasonably realistic representation of the local stress conditions. A continental crustal coefficient of friction $\mu = 0.8$ is used as is commonly found in metaigneous rocks and as was assumed for an investigation of regional stresses in the nearby town of Moodus (Moos and Zoback, 1990). Other values of the coefficient of friction ranging from 0.4 to 0.6 have been tested and show little difference in the spatial patterns of generated Coulomb stress changes (Ansari, 2018).

With assistance from Tom Nosal, we digitize elevation contours from the pre-excavation 1970 USGS GQ 1422 Plainfield quadrangle and superimpose those contours on the 2016 CT ECO data portal DEM to calculate the excavated quarry volume. A total volume $v = 4.05 \times 10^6$ m^3 of removed rock is determined with this method using ArcGIS tools. This translates into a total negative load $F = 1.11 \times 10^{11}$ N assuming a Quinnebaug mafic gneiss density $\rho = 2.8$ g/cm^3 and a vertical stress change of -0.57 MPa over the

Table 1

Element	Strike Length	Dip Length	# of Sub-elements		Strike	Dip	Boundary Code
			Along Strike	Along Dip			
Lake Char Fault	50 km	3 km	5	1	180	30	12
SE trending fault	6 km	2 km	1	1	118	90	12
Quarry	0.8 km	0.2 km	8	2	0	0	2

quarry area of 1.94×10^5 m^2. In the boundary element model, the quarry is represented by an area of 1.6×10^5 m^2 and an unload magnitude of -0.57 MPa is applied to each of 16 100x100 meter sub-elements. The quarry area is represented by a smaller area in the model to account for the fact that rock excavation in the quarry was not evenly distributed. The quarry depth starts at ground level at its northern entrance and increases to roughly 20 meters below the surface at its southern extent.

Different criteria have been used to characterize the conditions under which failure occurs in rocks. The Coulomb failure criterion requires that both the shear and normal stress on an incipient fault plane satisfy conditions analogous to those of friction on a preexisting surface. In the laboratory, confined rocks approximately obey the Coulomb failure conditions, which also appear to explain many field observations (Jaeger and Cook, 1979). Assuming a simple Coulomb friction model for earthquakes, the potential for slip will be enhanced or retarded by a change in the Coulomb failure stress, ΔCFS, as defined by:

$$\Delta CFS = \Delta\tau - \mu(\Delta\sigma_n - \Delta P_p) \quad (13)$$

in which $\Delta\tau$ is the change in shear stress resolved in the slip direction on the potential fault, $\Delta\sigma_n$ and ΔP_p are the changes in normal stress and pore pressure on the fault (positive for compression), and μ is the friction coefficient. Pore pressure is assumed hydrostatic. Thus, if $\Delta CFS > 0$, the slip potential is enhanced and if $\Delta CFS < 0$, it is inhibited (Scholz, 2002). Maximum and minimum principal stresses are derived from stress tensor outputs and rotated onto the fault plane to determine $\Delta\tau$ and $\Delta\sigma_n$ using Equations (3) and (4). Changes in Coulomb failure stress as a result of the unload are computed and plotted over a 15 x 15 km area around the quarry for two scenarios: 1) assuming a thrusting regime and fault geometry of the Lake Char Fault, and 2) assuming a strike-slip regime and fault geometry of the SE trending fault (Table 1).

3.0 Results

3.1 Geophysical Investigation of the Plainfield Subsurface

The gravity survey was conducted with the primary objective of reducing ambiguity in the geometry of significant faults in the area surrounding Wauregan Quarry. The relative gravity data were first reduced and mapped without correcting for the elevation errors that resulted from a faulty RTK GPS network connection. Due to the connection failure, measured elevations had uncertainties of ± 6 m, corresponding to errors of up to 1.85 mGal. Before correcting the elevation errors for each station to 1-meter LiDAR data, computed simple Bouguer anomaly contours appeared to be sporadically discontinuous. After making the correction, the plotted gravity values are more smooth and consistent (Fig. 11). A comparison between the figures demonstrates the sensitivity to accurate elevation data when reducing measured gravity values, and suggests that future surveys should consider avoiding the use of RTK GPS rovers as a

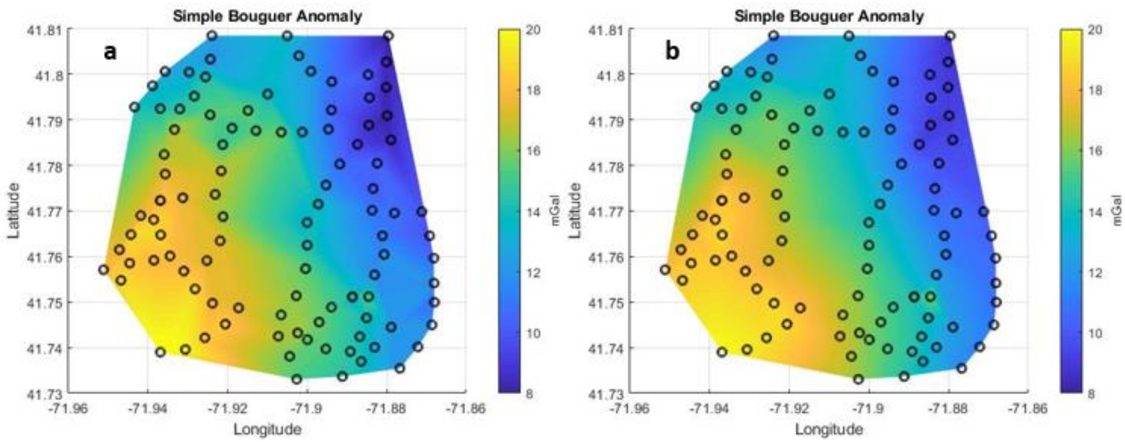

Fig. 11. Simple Bouguer anomalies processed from the 113 gravity measurements (black circles) collected in Plainfield, CT. The difference between the anomaly with inaccurately recorded RTK GPS elevations (a) and accurately measured elevations from LiDAR data (b) is most apparent along the yellow to green contour interface. Interpolated with Delaunay triangulation.

means of determining elevations if 1-meter resolution LiDAR data is available in the study area.

The Delaunay triangulation function in MATLAB, a "piecewise-linear" interpolation technique, was initially employed to generate the contour maps of the Bouguer gravity (Fig. 11). This algorithm interpolates with triangular surfaces by drawing lines between data points in such a way that no triangle edges are intersected by other triangles. However, this technique works best when data are evenly distributed over the grid area (Lee and Schachter, 1980). The inverse distance weighting (IDW) interpolation technique, an ArcMap 3D analyst tool, was found to be more effective given the relatively sparse distribution of gravity measurements in this research. IDW interpolation determines cell values using a linearly weighted combination of a set of sample points, where the weight is a function of inverse distance. The IDW interpolation of the simple Bouguer anomaly was spatially referenced and integrated with aeromagnetic data and geologic bedrock mapping in order to derive subsurface interpretations (Fig. 12).

When compared with bedrock geology mapping from Dixon (1965;1968), the simple Bouguer anomaly proved to serve as an effective representation of the subsurface based on inferred formation densities, and this enabled extrapolation of the extent of the southeast trending fault described earlier (Fig. 12). Calculated relative gravity values tend to decrease from west to east across the survey area. A maximum value of 20.0 mGal is seen in the southwest corner and a minimum value of 8.7 mGal is in the northeast. The southwestern part of the map in Figure 12 likely shows increased gravity values due to the mapped presence of a diopside-rich layer of the Black Hill Member, which is a fine-grained oligoclase schist of the Quinnebaug Formation. This part of the Black Hill Member outcrops just south of the southwestern extent of the survey area, but it probably lenses out to the north and south (Dixon 1965). The formation on the east side of the Lake Char Fault is primarily composed of the medium-grained Alaskite Gneiss, which is likely of lower density than most of the Quinnebaug Formation, based on its relatively light mineral content.

A negative region is apparent on the east side of the simple Bouguer anomaly and appears to trend N-S on strike with the Lake Char Fault (Fig. 12). Positive and negative anomalies have been observed in association with down-going slabs of modern subduction zones, dependent on thermal structure and the density of the down-going slab relative to the density of overlying material. Positive anomalies have been observed over the Aleutians and over the Chile trench west of South America, whereas negative anomalies have been known to be associated with oceanic trenches and island arcs (Garland, 1979). The Quinnebaug Formation is a thrust fault bound metaigneous island arc rock, which is separated from the Alaskite Gneiss to the east by the west-dipping Lake Char Fault. Because the Plainfield subsurface is in a tectonically passive margin, we do not consider the influence of thermal structure on gravity signature, and base interpretation on the juxtaposition of rocks of different densities due to shallow faults.

A method introduced by John M. Stanley (1977) was used to constrain dip angles of faults by using the gravity data:

$$\frac{(g''_{max} + g''_{min})}{(g''_{max} - g''_{min})} = \cos(\alpha) \tag{14}$$

where g''_{max} and g''_{min} are the maximum and minimum values of the second derivative of a gravity profile across a fault and α is the calculated dip angle. We applied the method of Eq. 14 to profile AB across the extrapolated extent of the southeast trending fault, which showed the presence of three closely spaced sub-vertical faults with an average dip of 87.5° SW. We additionally applied the method to a gravity profile taken perpendicular to the Lake Char Fault, but results were poorly resolved likely due to the shallow dip and length of the geologic contact. The dip angle of the Lake Char Fault is subsequently inferred based on published articles (Wilson, 1967) and aftershock geometry (Ebel, 2016). Historic aeromagnetic data supports structural interpretations made from the simple Bouguer map of this study. The extrapolation of the southeast trending sub-vertical fault to the southeast aligns with a ~500 meter left-lateral offset in a structure with relatively low magnetic susceptibility (Fig. 13). The same offset can be interpreted in the gravity data as contours that are abruptly deflected from N-S to NW-SE across the extended fault trace on the surface.

We consider the possibility that the southeast trending fault extends to and is crosscut by the Lake Char Fault. The aeromagnetic and gravity data do not appear to support this notion. Further southeastern extension of the fault does not seem warranted from the simple Bouguer map, although this may be due to the inherent thinning out – and subsequent reduction in resolution of structural information from gravimetry – of the Quinnebaug formation as it approaches the surface rupture of the west-dipping Lake Char Fault. In the aeromagnetic data, to the southeast of the previously mentioned negative anomaly structure that shows ~500 meters of left-lateral offset, there is a parallel positive anomaly structure that appears to coincide with the area of the quarry (Fig. 13). This positive anomaly structure is also in line to be intersected by the southeast trending fault, but it does not show corresponding evidence of significant left-lateral displacement (Fig. 13), which suggests that the fault terminates before intersecting with it.

Greater detail could have been achieved in the gravity survey with more evenly and closely distributed stations, although private property and bodies of water limited access in some areas. Additionally, higher resolution magnetic data would allow for further reduction in the uncertainty of the southeast trending fault extent. Regardless of these limitations, the left-lateral deflection of gravity and magnetic contours ceases abruptly at the inferred southeast trending fault extent (Fig. 12; Fig. 13), suggesting a discontinuation of the fault. Therefore, for the purposes of the Coulomb stress modelling in this study, we assume that the southeast trending fault stops about 1.2 km to the west of the northern end of the quarry, and does not intersect the Lake Char Fault.

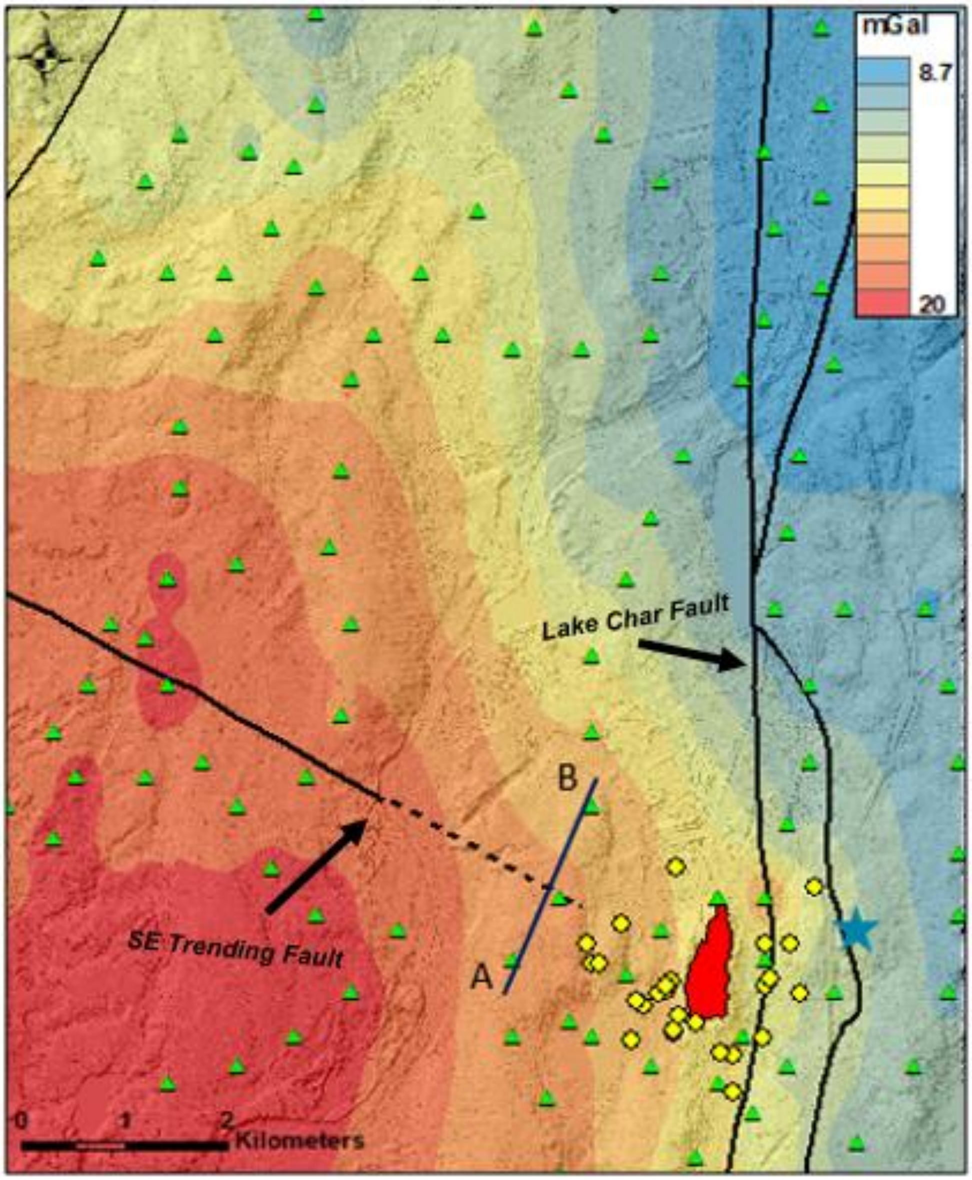

Fig. 12. Simple Bouguer anomaly over hillshade map processed from the 113 gravity measurements (green triangles) collected in Plainfield, CT. Solid black lines represent historically mapped faults; dashed black line is proposed extent of the southeast trending fault based on the geophysical data. Line AB is the gravity profile used to calculate dip of the southeast trending fault. Other symbols are the same as in previous figures.

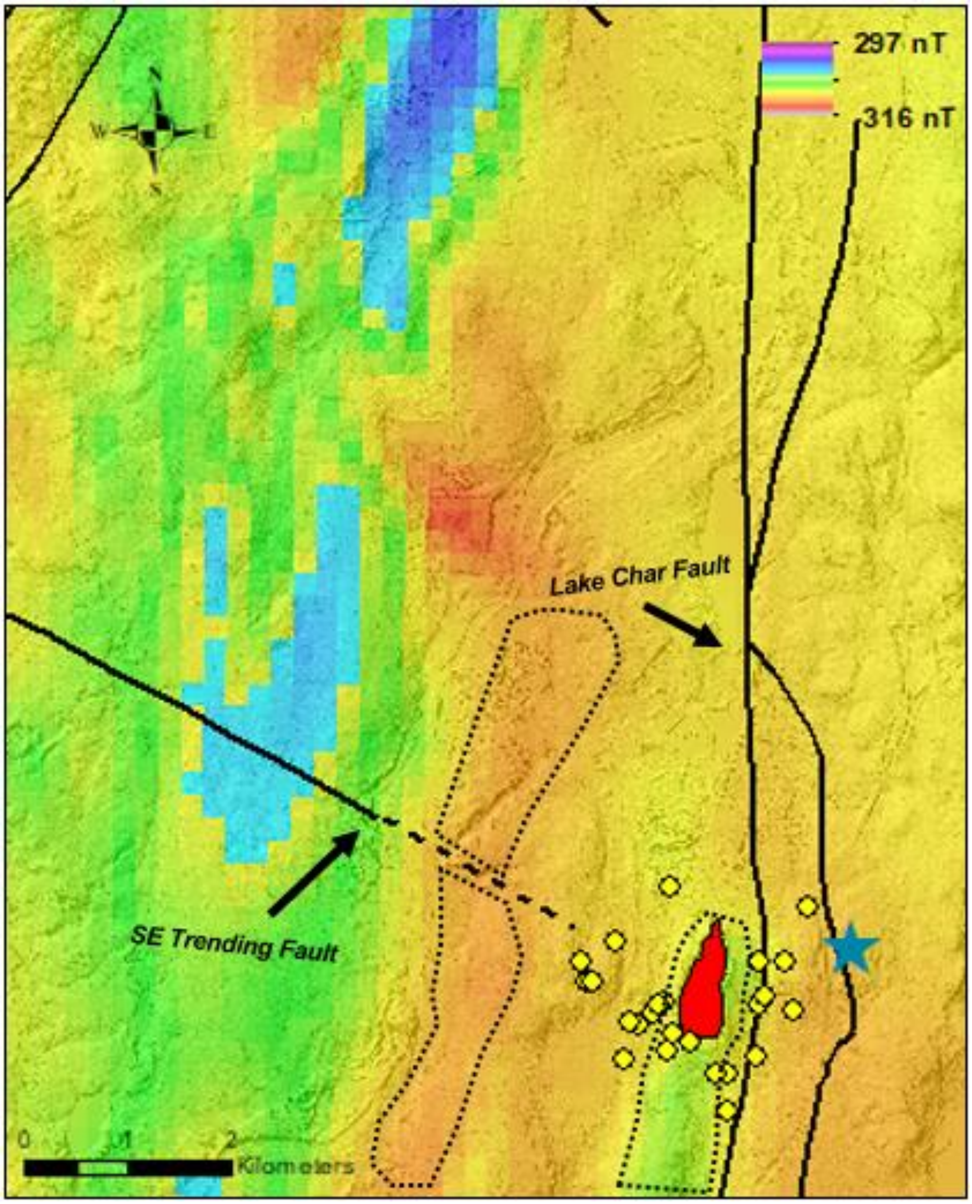

Fig. 13. Historic aeromagnetic data (Zietz et al., 1974) over hillshade map around the survey area in Plainfield, CT. Solid black lines represent historically mapped faults; dashed black line is proposed extent of the southeast trending fault based on the geophysical data. Dotted black lines highlight discussed anomalous structures in line with the southeast trending fault. Evidence of left-lateral slip is apparent in the west structure but not in the east. Other symbology is consistent with previous figures.

3.2 Modeling Coulomb failure stress on faults near Wauregan Quarry

Changes in Coulomb failure stress on the thrust and strike-slip faults near the quarry in Plainfield as a result of crustal unloading have been investigated with the 3D boundary element program – 3D~Def. Two models are analyzed: the first assumes a reverse faulting or thrusting regime and calculates ΔCFS using the geometry of the Lake Char Fault, and the second assumes a strike-slip regime and calculates ΔCFS using the geometry of the southeast trending fault. For both models, an unload of 0.57 MPa is applied over the quarry area. In addition to the orientations of the boundary element surfaces detailed in Table 1, Young's modulus $E = 5 * 10^8$ Pa, Poisson's ratio $\nu = 0.25$, and coefficient of friction $\mu = 0.8$ were used. Far-field stresses of $S_{Hmax} = 1.4 * 10^7$ Pa and $S_{hmin} = 1.0 * 10^7$ Pa are imposed at a depth of 100 meters for each model in top-view. An assumed lithostatic stress gradient was added to deviatoric stresses.

In the thrust ΔCFS model, Coulomb stress changes show correlations with the spatial distribution of aftershocks. As seen in past studies, aftershocks tend to preferentially occur in positive Coulomb stress zones and are less likely in the negative ones (Parsons et al., 2014; Lin and Stein, 2004). For the thrust model, 69% of the accurately located events occur in a 400 m-wide ring encircling the quarry, which represents the area of largest positive ΔCFS in the range of 0.01 – 0.8 MPa. According to King et al. (1994), it appears that static stress changes as low as 0.01 MPa can trigger seismicity. However, the stress changes shown (Fig. 14) are representative of conditions located hundreds of meters above the inferred west-dipping fault surface. The mapped mainshock location does not appear to fall within the region of highly positive ΔCFS, although its mapped location has an epicentral uncertainty of 2-3 kilometers. A total of

89% of the aftershocks occur in the positive Coulomb stress zones, with five of them located in a positive zone that shows ΔCFS of < +0.01 MPa. The remaining 11% of the aftershocks lie in a crescent-shaped lobe 800 m west of the quarry, with relatively small negative ΔCFS of > -0.01 MPa. A crescent-shaped lobe characterized by similarly negative ΔCFS values is mirrored 800 m to the east of the quarry.

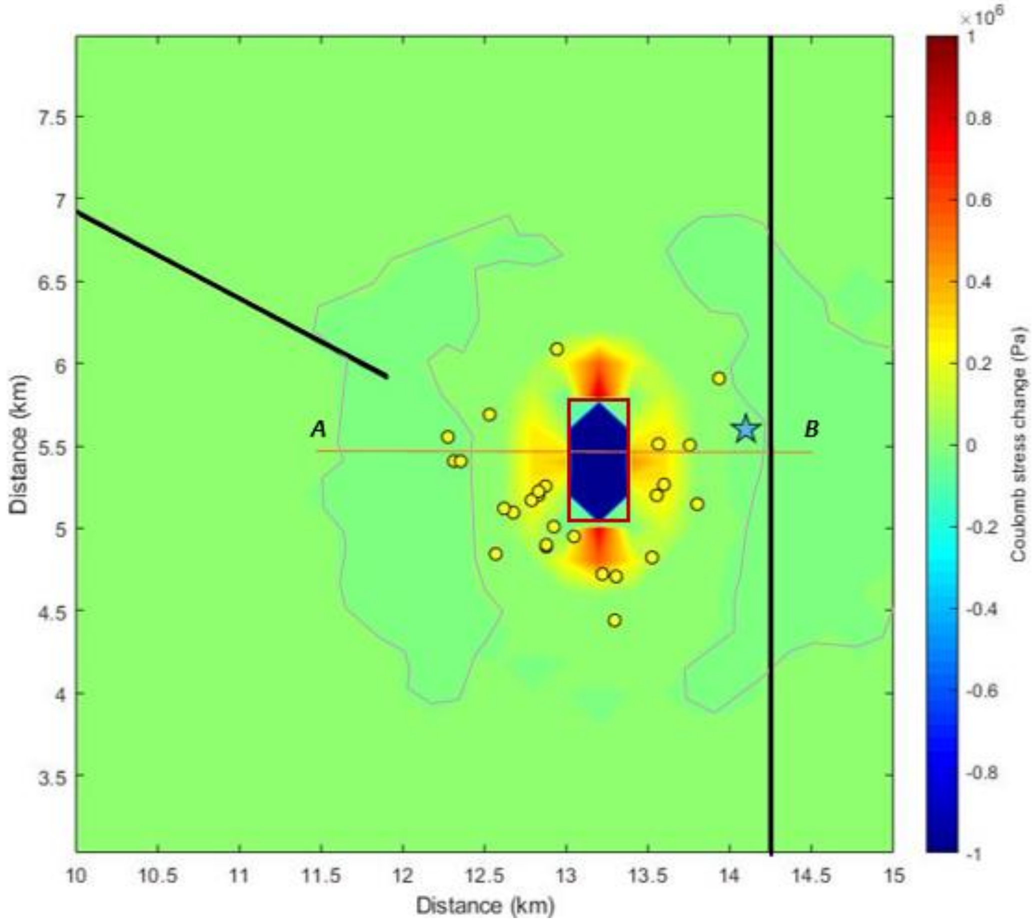

Fig. 14. Modeled ΔCFS for a thrusting regime on the west-dipping Lake Char Fault at a depth of 100 m, following a 0.57 MPa unload over the quarry area (red rectangle). ΔCFS values that are less than or equal to -1.0 MPa are dark blue; Positive ΔCFS values do not exceed 1.0 MPa. Crescent-shaped lobes of negative ΔCFS are outlined. Aftershocks are yellow circles. Mainshock location with epicentral uncertainty of 2-3 kilometers is represented by blue star. Line AB is a cross section shown in Fig. 15.

In the thrust model, a three km-long cross section – line AB (Fig. 14) – is taken E-W across the region containing the quarry area and aftershocks, parallel to the imposed S_{Hmax}. Figure 15 shows the cross section, enabling analysis of depth distribution and temporal development in the aftershocks relative to the ΔCFS zones. Three lobes of negative ΔCFS radially extend from the unload site into a subsurface characterized by generally positive ΔCFS. Minimum negative ΔCFS of -5.0 MPa and maximum positive ΔCFS of 0.8 MPa are seen in a 100 m radius extending below the unload site. ΔCFS magnitudes exponentially decrease with increasing distance from the unload site and are < |0.01| MPa at depths greater than 600 m. On the modeled Lake Char Fault surface, maximum ΔCFS of 0.01 – 0.05 MPa occur roughly 500 m below and 200 m east of the quarry area. In cross section, only 46% of aftershocks appear to occur in positive Coulomb stress zones. However, the figure shows a 2D representation of the 3D aftershock dataset, such that the apparent Coulomb stresses are not representative of conditions to the north or south. Seven of the first eight aftershocks align parallel to the modeled Lake Char Fault surface (Fig. 15) and appear to delineate a surface that is roughly 500 m deeper than the modeled west-dipping fault, with approximately the same dip angle. The focal depth of the mainshock was computed to be about 125 ± 96 m shallower than the fourth aftershock (Ebel, 2016; Fig. 15). Considering the uncertainties, the mainshock likely occurred at a depth of 0 – 100 m below the surface, which could have corresponded to ΔCFS > 0.1 MPa.

Of the 26 shown aftershocks, only events 1, 2, and 4 have M > 1 (Table 2; Fig. 2a; Fig 15). As time progressed over the course of the seven-month period in which aftershocks were recorded, the magnitudes tended to decrease; 54% of all accurately located aftershocks have M < 0 (Table 2). In Figure 2b, events 9-18 follow a trend on strike with the southeast oriented sub-vertical fault. This group of aftershocks seems to be randomly distributed with respect to depth, although it appears that the geometry of events 9, 10, 11, 12, 15, and 16 align in a sub-vertical fracture set that intersects with the west-dipping lineation defined by events 1-8 (Fig. 15). The aftershock lineation on strike with the southeast trending fault likely served as a preexisting weakness in the subsurface, which could have been activated with left-lateral slip to compensate for stress adjustments in the weeks following the mainshock thrust event. Coulomb failure stress changes from the quarry unload are computed for a left-lateral strike-slip regime in order to investigate this possibility (Fig. 16).

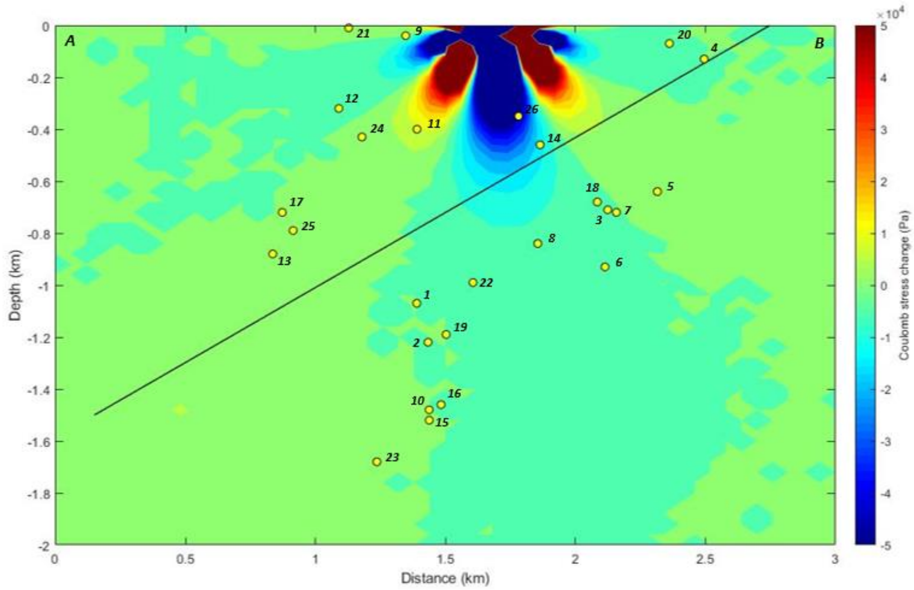

Fig. 15. Cross section of modeled Coulomb failure stress changes for a thrusting regime on the west-dipping Lake Char Fault from line AB in Figure 14. Black line is modeled Lake Char Fault surface. ΔCFS values that are greater than or equal to 0.05 MPa are dark red; ΔCFS values that are less than or equal to -0.05 MPa are dark blue. Yellow circles are aftershocks numbered as they occurred chronologically.

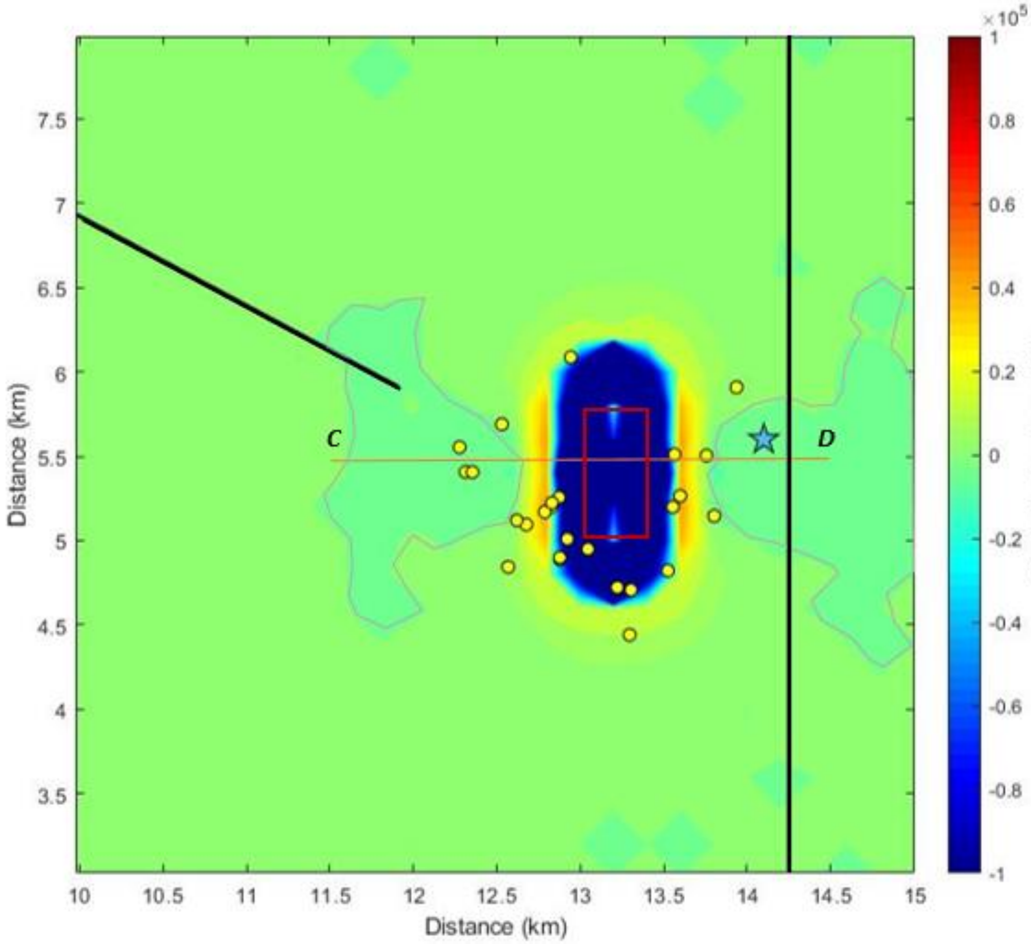

Fig. 16. Modeled ΔCFS for a strike-slip regime assuming geometry of the southeast trending sub-vertical fault at a depth of 100 m, following a 0.57 MPa unload over the quarry area (red rectangle). ΔCFS values that are less than or equal to -0.1 MPa are dark blue; Positive ΔCFS values do not exceed 0.1 MPa. Crescent-shaped lobes of negative ΔCFS are outlined. Aftershocks are yellow circles. Mainshock location with epicentral uncertainty of 2-3 kilometers is represented by blue star. Line CD is a cross section shown in Fig. 17.

The ΔCFS model for left-lateral strike-slip shares notable similarities with the thrust ΔCFS model, particularly in the spatial distribution of Coulomb stresses. A 200 m-wide ring of positive ΔCFS in the range of 0.01 – 0.05 MPa lies around the perimeter of an 800 x 1600 m rectangular zone of negative ΔCFS that encapsulates the quarry area (Fig. 16). Additionally, two lobes of negative ΔCFS of > -0.01 MPa are mirrored 600 m to the west and east of the quarry area. However, only 27% of the aftershocks occur in positive Coulomb stress zones (Fig. 16) as compared to the 89% seen in the Lake Char Fault ΔCFS model (Fig. 14). In cross section, minimum negative ΔCFS of -0.9 MPa and maximum positive ΔCFS of up to 0.3 MPa are seen in a 100 m radius below the unload site (Fig. 17). ΔCFS of the order of 0.001 MPa occur beyond a radius of 500 m from the unload site. Aftershocks that align with the southeast trending fault (Fig. 2b), including events 9, 10, 11, 12, 15, and 16 appear to occur primarily in positive Coulomb stress zones with maximum ΔCFS of 0.003 MPa (Fig. 17).

In general, within a 500 m radius from the quarry, ΔCFS as a result of the 0.57 MPa unload are roughly an order of magnitude smaller in the strike-slip fault model than in the thrust model. These results suggest that it is possible that aftershocks in line with the southeast trending fault could have been activated with left-lateral slip to compensate for stress adjustments in the weeks following the mainshock thrust event. Positive ΔCFS seen in the southeast trending fault model are small, but greater than 0.01 MPa near the surface, which suggests that the static stress changes could be large enough to trigger aftershock development (King et al., 1994) with left-lateral strike-slip motion. However, Coulomb stress changes that exceed 0.01 MPa do not coincide with the modeled position of the southeast trending fault surface. A possible explanation for this discrepancy is that unknown faults, which are not incorporated in the model in this study, align more closely with areas of $\Delta CFS > 0.01$ MPa and account for the southeast trend in aftershock distribution. Furthermore, it is possible that the modeled extent of the southeast trending fault is inaccurate, and that the fault does in fact extend further toward the Lake Char Fault, in line with the southeast trend in aftershocks 9-18 (Fig. 2b).

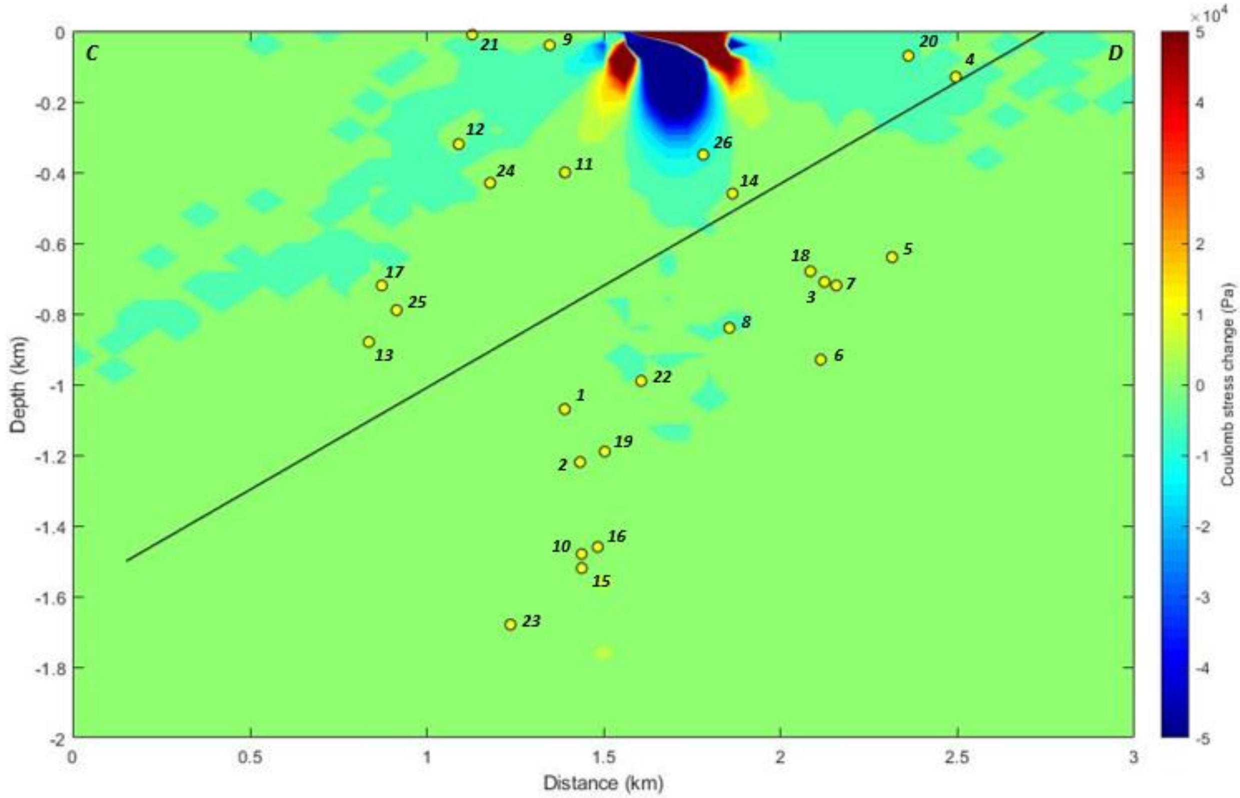

Fig. 17. Cross section of modeled Coulomb failure stress changes for a strike-slip regime assuming geometry of the southeast trending sub-vertical fault from line CD in Figure 16. Black line is modeled Lake Char Fault surface. ΔCFS values that are greater than or equal to 0.05 MPa are dark red; ΔCFS values that are less than or equal to -0.05 MPa are dark blue. Yellow circles are aftershocks numbered as they occurred chronologically.

Table 2

Event #	Date	Time	Lat °N	Long °E	Depth (km)	RMS (sec)	Mag.*
1	1/14/15	11:33	41.7450	-71.8937	1.07	0.01	1.7
2	1/14/15	13:10	41.7455	-71.8932	1.22	0.02	1.1
3	1/15/15	9:33	41.7480	-71.8850	0.71	0.01	-0.1
4	1/15/15	9:39	41.7517	-71.8807	0.13	0.02	1.9
5	1/15/15	10:11	41.7480	-71.8827	0.64	0.01	0.4
6	1/15/15	22:50	41.7452	-71.8850	0.93	0.01	0.5
7	1/16/15	0:09	41.7458	-71.8845	0.72	0.00	0.2
8	1/17/15	0:18	41.7383	-71.8878	0.84	0.01	0.0
9	1/22/15	4:39	41.7447	-71.8942	0.04	0.03	0.0
10	1/23/15	5:16	41.7422	-71.8930	1.48	0.01	-0.8
11	1/23/15	5:36	41.7452	-71.8937	0.40	0.02	0.1
12	2/13/15	20:33	41.7493	-71.8975	0.32	0.01	0.1
13	2/17/15	9:21	41.7480	-71.9005	0.88	0.01	-1.1
14	2/19/15	12:54	41.7407	-71.8878	0.46	0.00	0.4
15	2/19/15	13:08	41.7423	-71.8930	1.52	0.01	-0.2
16	2/19/15	15:13	41.7433	-71.8925	1.46	0.01	-1.0
17	2/25/15	9:33	41.7467	-71.9000	0.72	0.00	-0.9
18	3/1/15	10:08	41.7418	-71.8852	0.68	0.01	-1.0
19	3/8/15	13:34	41.7530	-71.8927	1.19	0.03	0.2
20	3/22/15	8:51	41.7448	-71.8820	0.07	0.04	-1.0
21	5/1/15	4:01	41.7417	-71.8967	0.01	0.01	-0.5
22	5/3/15	23:14	41.7428	-71.8910	0.99	0.02	-1.3
23	5/8/15	10:16	41.7440	-71.8955	1.68	0.01	-1.2
24	5/9/15	9:34	41.7442	-71.8962	0.43	0.02	-0.6
25	5/22/15	7:36	41.7467	-71.8995	0.79	0.02	-0.7
26	7/13/15	4:35	41.7408	-71.8888	0.35	0.01	-1.2

*** Magnitude computed from the maximum amplitude at station 9CCD.**

4.0 Discussion

The idea that crustal unloading from quarrying can induce seismicity is not new; however, only a few cases have been published in the literature. The Plainfield swarm of 2015 provides a unique opportunity to investigate this phenomenon with an unusually detailed data set. From geologic mapping and geophysical data, we imaged two significant faults, a southeast trending sub-vertical fault and the west-dipping Lake Char Fault, the latter of which was likely involved in the onset of seismicity in a roughly 2 x 2 km area around Wauregan Tilcon Quarry. In a thrusting regime (Fig. 6) as is seen throughout the northeastern U.S. (Fig. 8), decreasing the lithostatic load, or minimum principal stress (σ_3), shifts a Mohr-Coulomb diagram toward failure (Fig. 7). This concept is supported by the results from the thrusting regime ΔCFS model, which suggests quarry excavation brought the Lake Char Fault closer to failure (Fig. 14) and contributed to the onset of the seismicity that took place in the 2015 swarm.

In a strike-slip regime, the lithostatic load is the intermediate principal stress (σ_2), which does not affect the Mohr-Coulomb failure criterion (Simpson, 1986). Thus, it is not surprising that significantly smaller ΔCFS resulted from crustal unloading in the strike-slip ΔCFS model (Fig. 16). However, the optimal angle for frictional sliding, with coefficient of friction $\mu = 0.8$, is $\beta = 37^\circ$ (Eq. 6), independent of stress regime. Relative to the imposed S_{Hmax}, the orientations of both the southeast trending strike-slip fault ($\theta = 28^\circ$) and the Lake Char Fault ($\theta = 30^\circ$) are nearly optimal. With optimally oriented regional stresses and small enough distance between the faults, Wang et al. (2013) showed that strike-slip faults can be triggered and then rupture completely as a result of the failure of a nearby thrust fault. Although ΔCFS associated with the strike-slip model are small and the southeast trending fault does not coincide with regions of ΔCFS > 0.01 MPa (Fig. 16), it is possible that the fault position is not accurately represented in the model. If the southeast trending fault does in fact extend further southeast to intersect the Lake Char Fault – or if another undetected high angle fault exists near the southwestern edge of the quarry – the aftershocks that developed on trend with the southeast trending fault could have been triggered with strike-slip failure in order to compensate for stress adjustments following the mainshock.

In addition to the possibility of strike-slip faulting, aftershock geometry and results from boundary element modeling suggest the possibility of back thrust faulting and the formation of a pop-up structure following the mainshock. A pop-up structure is a structurally uplifted block bounded by thrust faults with opposing senses of motion (McClay, 1992). Figure 14 shows largely positive ΔCFS for thrust faulting immediately surrounding the quarry with negative ΔCFS lobes mirrored 800 m to its west and east. In a setting confined by a horizontal maximum principal stress, the mirrored contrast between positive and negative ΔCFS interfaces seen on either side of the quarry (Fig. 14) could ostensibly encourage the development of opposing senses of thrust motion. Aftershock events 9, 10, 11, 15, and 16 delineate a high-angle plane that dips steeply east, which intersects the surface about 100 m west of the quarry. This east-dipping plane intersects the west-dipping plane delineated by events 1-8 beneath the quarry, inferred to be approximately representative of the Lake Char Fault surface (Fig. 15). The geometry of the planes delineated by these aftershocks appear to suggest that the opposing sides of a pop-up structure might be defined by the Lake Char Fault surface on the east, and the steeply east-dipping plane on the west.

The 1994 Cacoosing Valley, PA and 1974 Wappingers Falls, NY earthquakes represent two of the few cases of potentially quarry-induced seismicity in the northeastern U.S. that have been investigated scientifically. Remarkable similarities exist between these events and the 2015 Plainfield earthquakes. In all three cases, mainshocks and aftershocks occur within a ~3 km radius from the center of each respective quarry. The Cacoosing Valley mainshock focal mechanism suggests a thrusting fault plane with strike 135˚ (Seeber et al., 1998) as compared to the fault strikes of 120˚ and 15˚ seen in the area around Wauregan Quarry. Cacoosing Valley, PA is ~400 km southwest of the Plainfield area, but considering the far-field influences that determine intraplate stress orientations, similarity in maximum principal stresses at these distances is reasonable (Sbar and Sykes, 1974; Fig 16). The NE-SW oriented S_{Hmax} shown trending throughout the northeast United States (Ebel and Kafka, 1991; Hurd and Zoback, 2012; Fig. 8) supports this notion. The first studied instance of proposed quarry-induced seismicity occurred under a surface quarry in Wappingers Falls (Pomeroy et al., 1976), where a magnitude 3.3 event occurred ~200 km northeast of the Cacoosing sequence along strike of the Appalachians thrust belt. The focal mechanism computed for this event suggests a thrusting fault plane with strike 130˚ and dip 60˚ SW (Fig. 18). The composite fault-plane solutions for mainshocks and well-located aftershocks for the events at Cacoosing Valley, Wappingers Falls, and Plainfield are all indicative of thrusting mechanisms (Fig. 18). Additionally, in all three cases, the mainshock events are preceded by foreshocks and followed by swarms of hundreds of aftershocks, which all occur within the upper 2.5 km of the crust.

The largest earthquakes of the three documented locations were magnitudes 4.0 and 4.6. Both of these events occurred in 1994 in Cacoosing Valley, PA with the smaller preceding the larger by an hour. However, the volume of extracted material from the Cacoosing Valley quarry ($4.0x10^6$ m^3) was roughly the same as the volume removed from the Plainfield quarry ($4.05x10^6$ m^3), and smaller than that removed from the Wappingers Falls quarry ($2.5x10^7$ m^3). In Cacoosing Valley, about a month before the 1994 mainshock in January, quarry operations were stopped and the quarry was filled with water. Seeber et al. (1998) suggested that the increase in pore pressure associated with the flooding of the quarry largely contributed to his calculated 0.13 MPa increase in coulomb stress toward failure, serving as a possible explanation for the relatively large seismic events. The Plainfield and Wappingers Falls quarries were never excavated below the water table and thus have not been at risk of flooding. In Plainfield, quarry operations stopped in 2011, and no earthquakes were detected from the Wauregan area prior to 2014, including during the years when the quarry was active. The first recorded seismic activity in the area occurred on 13 October, 2014 with an earthquake of magnitude 0.9, followed by two additional earthquakes of similar magnitude on 9 November, 2014. One possible explanation for the gap in time between the end of quarry operations and the onset of seismicity is that the unloading modified the natural cycle of stress release.

Through various tectonic processes, the state of stress in the Earth's crust changes as a function of time (Sykes and Sbar, 1973). Industrial activities, such as quarrying, modify the natural cycle of stress release so that earthquakes can be "triggered" many years before they would have naturally occurred (Simpson, 1986). The stress changes

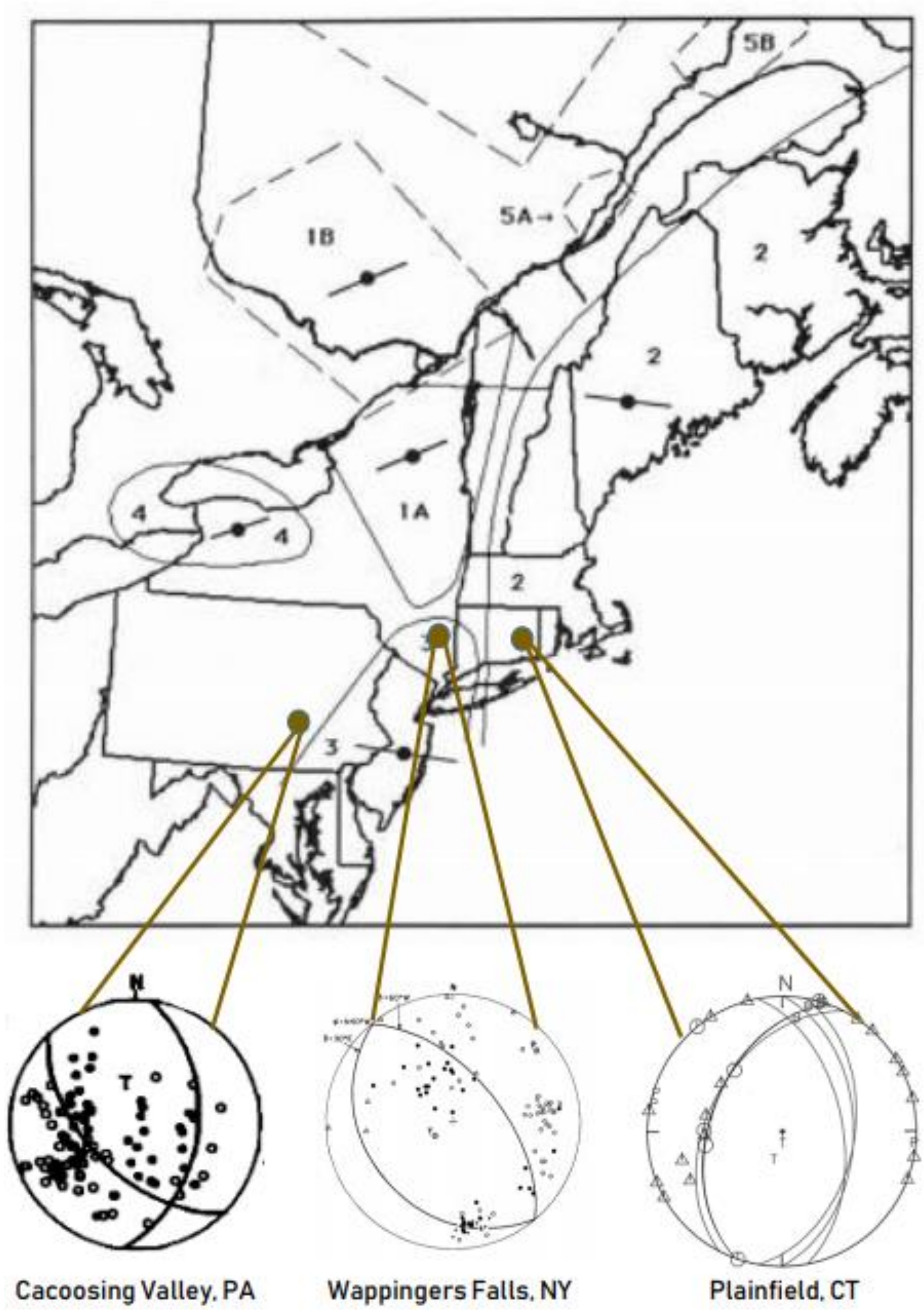

Fig. 18. Map of the northeastern United States with numbered seismic zones and average P-axis azimuths for each zone [from Ebel and Kafka, 1991]. Total average P-axis trend of 86° ± 40° is calculated for the entire region. Focal plane mechanisms determined for the Plainfield (Ebel, 2016), Cacoosing Valley (Seeber et al., 1998), and Wappingers Falls (Pomeroy et al., 1976) mainshocks suggest thrusting events that tend to strike roughly perpendicular to the average P-axis trend.

induced by the quarries in Cacoosing Valley and Wappingers Falls are small compared to the level of stress expected to cause seismogenic failure (Seeber et al., 1998; Pomeroy et al., 1976) and the same can be said for the Wauregan Quarry. Given that natural seismicity in stable continental regions has a minimum recurrence interval of 10^5 years (Crone and Machette, 1992), it is possible that crustal unloading in Plainfield accelerated the rate of natural seismicity, bringing the stress conditions on the fault very close to the friction limit (Eq. 5).

A shallow magnitude 4.2 thrust earthquake occurred in the Eastern Sichuan Basin of China in 2016, which was likely triggered by crustal unloading during infrastructure construction (Qian et al., 2019). Similar to the Plainfield mainshock, the Sichuan Basin earthquake did not occur until ~2 years after the construction was completed. Qian et al. (2019) suggest that the delayed triggering might be a result of removal of vegetation cover during construction, allowing surface water to migrate and increase pore pressure at depth. At Wauregan Quarry, removal of vegetation cover would have been necessary before operations began, and thus might have contributed to the timing of the Plainfield swarm. However, the extent to which this process would have influenced the timing of delayed triggering is unknown and requires further investigation. Additionally, the time between removal of vegetation cover and the onset of seismicity in the Sichuan Basin was roughly 3 years (Qian et al., 2019), whereas the same period would have been upwards of 35 years in Plainfield.

If we assume that delayed triggering occurs strictly as a result of the natural seismicity cycle, we can use a regional strain rate to determine the amount of time that corresponds to a given amount of ΔCFS on an intraplate fault. For simple geometry, the equation for rate of shear stressing on a fault is given by:

$$\tau' = \frac{\mu_r v}{\pi w} \tag{15}$$

where τ' is the rate of shear stressing on the fault, μ_r is the rigidity, v is the loading rate, and w is the vertical extent of the seismogenic fault (Stein and Liu, 2009). Assuming $\mu_r = 2.0 * 10^{10}$ Pa, $v = 0.2$ mm/yr for eastern North America (Mazzotti et al., 2005), and $w = 2$ km in Plainfield, the rate of shear stressing on the Lake Char Fault is $\tau' \approx 600$ Pa/yr. With ΔCFS on the Lake Char Fault of 0.01 – 0.1 MPa after the quarry excavation, it follows that the recurrence of natural seismicity on the fault was advanced by 17 to 170 years, and the ~3 year period between the end of quarry operations in 2011 and the onset of seismicity in 2014 corresponded to an increase of ~0.002 MPa. In other words, regardless of whether crustal unloading had taken place at Wauregan Quarry or not, it is possible that seismicity would have occurred naturally on the Lake Char Fault within the next ~170 years anyway.

5.0 Conclusions

The 2015 Plainfield swarm of earthquakes took place in the area immediately around Wauregan Quarry. Quarrying operations caused a reduction in lithostatic load of 1.11×10^{11} N from the upper crust, which affected the stresses in the subsurface. The distribution of accurately located aftershocks appears to delineate rupture geometries corresponding to two sub-perpendicular trends: the west-dipping Lake Char Fault complex that strikes 15˚, and the fault trending southeast that strikes 123˚. Results from the gravity survey provide evidence to support the notion that the Lake Char Fault is a shallowly west dipping geologic suture separating higher density metaigneous island arc rocks in the west from the Precambrian Alaskite Gneiss to the east. Gravity and aeromagnetic data provide an updated estimate of the extent of the southeast trending fault, suggesting that the fault terminates before intersecting the subsurface beneath the quarry, and supporting historic mapping.

Two Coulomb stress models were produced with a 3D boundary element program to analyze ΔCFS resulting from the quarry unload in Plainfield. The first assumes a thrusting regime and calculates ΔCFS using the geometry of the Lake Char Fault, and the second assumes a strike-slip regime and calculates ΔCFS using the geometry of the southeast trending fault. Both models suggest that ΔCFS > 0.01 were produced on the corresponding fault surfaces and hence large enough to trigger seismicity. The thrust ΔCFS model shows that stress changes of > 0.05 MPa occurred at depths down to 400 m beneath the unload site and approach a max of 0.8 MPa near the surface. The strike-slip ΔCFS model shows stress changes that are roughly an order of magnitude smaller than those of the thrust model; ΔCFS of > 0.005 MPa occur at depths down to 400 m beneath the unload site and approach a max of 0.3 MPa near the surface. Given that thrust faulting is capable of triggering nearby strike-slip faults (Wang et al., 2013), it is possible that the aftershocks on strike with the southeast trending fault occurred with left-lateral slip to compensate for stress adjustments in the weeks following the mainshock thrust event. However, this would suggest that the modeled position of the strike-slip fault extends further southeast than its current estimated termination, or that a separate undetected high-angle fault exists near the southwestern corner of the quarry. Further explanation of the aftershock distribution might be accounted for by the potential formation of a pop-up structure with back thrust faulting west of the quarry.

The thrust ΔCFS model was the preferred model and suggests that crustal unloading as a result of the quarry excavation contributed to the triggering of the magnitude 3.1 Plainfield mainshock on the Lake Char Fault. The majority of the accurately located aftershocks (89%) lie within positive Coulomb stress zones when observing the model from map view (Fig. 14), suggesting that the unloading due to excavation of the quarry probably had an influence on the spatial distribution of the swarm. The focal mechanism computed from the mainshock suggests thrusting on a plane that is parallel to the Lake Char Fault and sub-perpendicular to the regional maximum principal stress. Failure is expected at a differential stress of 30 MPa on an ideally oriented fault at a depth of 1 km if σ_3 is vertical and equal to the overburden, pore pressure is hydrostatic, and friction is consistent with laboratory results (Seeber et al., 1998). In this scenario, the differential stress was likely very close to failure before quarry operations began, and brought even closer to failure by the time they stopped in 2011. In agreement with past studies, the results of this study suggest that quarrying operations can trigger seismic activity in specific settings with a favorable stress regime, fault orientations, and rock characteristics such as those that exist in the northeastern U.S. In order to mitigate the risk for future earthquakes related to quarrying operations, these factors must be considered before operations begin.

References

Anderson, E.M., 1951, The Dynamics of Faulting, Edinburgh: Oliver and Boyd.

Ansari, S., 2018, Stress triggering and aftershock properties induced by the Dalparri blind thrust fault at NW Zagros: The 18 August 2014 Mormori earthquake: Global and Planetary Change, v. 167, pp. 99-109.

Burger, H.R., Sheehan, A.F., and Jones, C.H., 2006, Introduction to Applied Geophysics: Exploring the Shallow Subsurface, W. W. Norton & Company, Inc., New York, NY, USA.

Crone, A.J., Machette, M.N., and Bowman, J.R., 1992, Geologic investigations of the 1988 Tennant Creek, Australia, earthquakes: Implications for seismicity in stable continental regions: US. Geol. Surv. Bull. v. 2032-A, pp. 51.

Dixon, H.R., 1965, Bedrock geologic map of the Plainfield quadrangle, Windham and New London Counties, Connecticut: U.S. Geological Survey, Geologic Quadrangle Map GQ-481, scale 1:24,000.

Dixon, H.R., 1968, Bedrock geologic map of the Danielson quadrangle, Windham County, Connecticut: U.S. Geological Survey, Geologic Quadrangle Map GQ-696, scale 1:24,000.

Doglioni, C., 2018, A classification of induced seismicity: Geoscience Frontiers, v. 9, no. 6, pp. 1903-1909.

Ebel, J.E., 2006, The Cape Ann, Massachusetts Earthquake of 1755: A 250th Anniversary Perspective: Seismological Research Letters, v. 77, no. 1, pp. 74-86.

Ebel, J.E., 2016, Plainfield Earthquakes: Weston Observatory, Boston College [unpublished paper].

Ebel, J.E., 1989, A comparison of the 1981, 1982, 1986, and 1987-1988 microearthquake swarms at Moodus, Connecticut: Seismological Research Letters, v. 60, no. 4, pp. 177-184.

Ebel, J.E. and Kafka, A.L., 1991, Earthquake activity in the Northeastern United States: Neotectonics of North America, D.B. Slemmons, E.R. Engdahl, M.D. Zoback, and D.D. Blackwell, The Geological Society of America, Decade Map, v. 1, pp. 277-290.

Ekstrom, G., Stein, R.S., Eaton, J.P., Eberhart-Philips, D., 1992, Seismicity and geometry of a 110-km long blind thrust fault, 1, the 1985 Ketlleman Hills, California, earthquake, Journal of Geophysical Research, v. 97, pp. 4843-4864.

Garland, G.D., 1979, Introduction to Geophysics, W. B. Saunders Company, Philadelphia, PA, USA.

Gibowitz, S.J., 1982, The mechanism of large mining tremors in Poland: Proc. Int. Congr. Rockbursts and Seism. in Mines, 1st, ed. N. C. Gay, E. H. Wainwright, pp. 17-28.

Gomberg, J. and M. Ellis, 1994, Topography and tectonics of the central New Madrid seismic zone: Results of numerical experiments using a three-dimensional boundary-element program: J. Geophys. Res., v. 99, pp. 20,299-20,310.

Growdon, M.L. and Byrne, T., 2005, Post-faulting deformation of the Lake Char-Honey Hill Fault, southeastern Connecticut: Geological Society of America, Northeastern Section, 40th annual meeting, v. 37, no. 1, pp.83.

Gupta, H.K., 2002, A review of recent studies of triggered earthquakes by artificial water reservoirs with special emphasis on earthquakes in Koyna, India: Earth-Science Reviews, v. 58, pp. 279-310.

Heidbach, O., Rajabi, M., Reiter, K., Ziegler, M.; WSM Team, 2016: World Stress Map Database Release 2016. V. 1.1. GFZ Data Services.

Hurd, O., and Zoback, M.D., 2012, Intraplate earthquakes, regional stress and fault mechanics in the Central and Eastern U.S. and Southeastern Canada: Tectonophysics, v. 581, pp. 182-192.

Jaeger, J.C., and Cook, N.G.W., 1979, Fundamentals of Rock Mechanics, 3rd ed., Chapman and Hall, London.

Kafka, A.L., Schlesinger-Miller, E.A., and Barstow, N.L., 1985, Earthquake activity in the greater New York City area: magnitudes, seismicity, and geologic structures: Bulletin of the Seismological Society of America, v. 75, no. 5, pp. 1285-1300.

King, G.C.P., Stein, R.S., and Lin, J., 1994, Static Stress Changes and the Triggering of Earthquakes: Bulletin of the Seismological Society of America, v. 84, no. 3, pp. 935-953.

Kozłowska, M., Orlecka-Sikora, B., Kwiatek, G., Boettcher, M.S., and Dresen, G., 2015, Nanoseismicity and picoseismicity rate changes from static stress triggering caused by a Mw 2.2 earthquake in Mponeng gold mine, South Africa: J. Geophys. Res. Sol Ea., v. 120., pp. 290-307.

Lee, D.T., and Schachter, B.J., 1980, Two algorithms for constructing a Delaunay triangulation: International Journal of Computer & Information Sciences, v. 9, pp. 219-242.

Lin, J. and Stein, R.S., 2004, Stress triggering in thrust and subduction earthquakes and stress interaction between the southern San Andreas and nearby thrust and strike-slip faults: Journal of Geophysical Research, v. 109, B02303.

Mazzotti, S., James, T.S., Henton, J., and Adams, J., 2005, GPS crustal strain, postglacial rebound, and seismic hazard in eastern North America: The Saint Lawrence valley example: Journal of Geophysical Research: Solid Earth, v. 110, B11.

McClay, K.R., 1992, Glossary of thrust tectonic terms: Thrust Tectonics, Chapman and Hall, pp. 419-433.

McDonald, M.R., 2013, Geophysical investigation and assessment of the Rye Patch known geothermal resource area, Rye Patch, Nevada: PhD dissertation, University of North Dakota.

Moos, D. and Zoback, M.D., 1990, Utilization of Observations of Well Bore Failure to Constrain the Orientation and Magnitude of Crustal Stresses: Application to Continental, Deep Sea Drilling Project, and Ocean Drilling Program Boreholes: Journal of Geophysical Research, vol. 95, no. B6, pp. 9305-9325.

Nowell, D.A.G., 1999, Gravity terrain corrections – an overview: Journal of Applied Geophysics, v. 42, pp. 117-134.

Parsons, T., Segou, M., Sevilgen, V., Milner, K., Field, E., Toda, S., and Stein, R.S., 2014, Stress-based aftershock forecasts made within 24 h post main shock: expected north San Francisco Bay area seismicity changes after the 2014 M=6.0 West Napa earthquake: Geophysical Research Letters, v. 41, pp. 8792-8799.

Pomeroy, P.W., Simpson, D.W., and Sbar, M.L., 1976, Earthquakes triggered by surface quarrying – The Wappingers Falls, New York sequence of June, 1974: Bulletin of the Seismological Society of America, v. 66, no. 3, pp. 685-700.

Rodgers, John, 1985, Bedrock geological map of Connecticut: Connecticut Geological and Natural History Survey, Connecticut Natural Resources Atlas Series, scale 1:125,000, 2 sheets.

Scholz, C.H., 2002, The Mechanics of Earthquakes and Faulting, Cambridge University Press, Cambridge, UK.

Seeber, L., Armbruster, J.G., Kim, W.Y., and Barstow, N., 1998, The 1994 Cacoosing Valley earthquakes near Reading, Pennsylvania: A shallow rupture triggered by quarry unloading: Journal of Geophysical Research, v. 103, no. B10, pp. 24505-24521.

Sibson, R.H., 1985, Stopping of earthquake ruptures at dilatational jogs: Nature, v. 316, pp. 248-251.

Simpson, D.W., 1986, Triggered Earthquakes: Annual Review of Earth and Planetary Sciences, v. 14, pp. 21-42.

Stanley, J.M., 1977, Simplified gravity interpretation by gradients – The geological contact: Geophysics, v. 42, no. 6, pp. 1230-1235.

Stein, S. and Liu, M., 2009, Long aftershock sequences within continents and implications for earthquake hazard assessment: Nature, v. 462, pp. 87-89.

Sykes, L.R., and Sbar, M.L., 1973, Intraplate Earthquakes, Lithospheric Stresses and the Driving Mechanism of Plate Tectonics: Nature, v. 245, no. 5424, pp. 298-302.

Thomas, M., 2019, Wauregan Quarry area geologic summary: Connecticut Geological Survey, Dept. of Energy and Environmental Protection.

Wang, J.C., Shieh, C., and Wang., J., 2013, A Study of Interactions between Thust and Strike-slip Faults: Terrestrial, Atmospheric and Oceanic Sciences, v. 24, no. 5, pp. 809-825.

Weingarten, M., Ge, S., Godt, J.W., Bekins, B.A., and Rubinstein, J.L., 2015, High-rate injection is associated with the increase in U.S. mid-continent seismicity: Science, v. 348, no. 6241, p. 1336-1340.

Wilson, J.T., 1966, Did the Atlantic close and then re-open? Science, v. 211, no. 5050, pp. 676-681.

Yan, J., Wang, Z., Wang, J., and Song, J., 2018, Using marine magnetic survey to identify a gold ore-controlling fault: a case study in Sanshandao fault, eastern China: J. Geophys. Eng., v. 15, pp. 729-738.

Zietz, Isidore, Kirby, J.R., Jr., and Gilbert, F.P., 1974, Aeromagnetic Map of Connecticut: U.S. Geological Survey Geophysical Investigations Map GP-897, scale 1:125,000.

Zoback, M.D., 2007, Reservoir Geomechanics, Cambridge University Press, New York, NY, USA.

Zoback, M.D. and Zoback M.L., 1991, Tectonic stress field of North America and relative plate motions: The Geology of North America, Decade Map Volume 1, Neotectonics of North America, Geol. Soc. Am., Boulder, Colorado, pp. 339-366.

Appendix

Gravity Survey Data

Table 3

***BASE STATIONS ARE HIGHLIGHTED**

STATION	Latitude	Longitude	Bad Elevation (m)	Corrected Elevation (m)	Raw Gravity Data (mGal)	Simple Bouguer (mGal)
1	41.751	-71.889	72.1748	72.1	-0.008	14.182
2	41.751	-71.885	69.8758	72.7	1.488	15.782
3	41.756	-71.883	72.2544	74.9	-2.02	12.266
4	41.76	-71.881	74.5249	70.4	-1.662	11.331
5	41.765	-71.881	74.1307	73.7	-2.214	11.048
6	41.77	-71.884	79.122	78	-2.808	10.779
7	41.77	-71.878	109.3737	109.3737	-9.001	10.81
8	41.749	-71.894	66.4088	64.9	2.044	14.911
9	41.746	-71.897	69.8614	69.2	1.594	15.584
10	41.751	-71.889	69.1635	72.1	0.113	14.184
11	41.747	-71.885	75.6129	74.4	-1.192	13.677
12	41.745	-71.879	75.7657	76.3	-3.111	12.316
13	41.742	-71.887	74.8192	74.8192	-1.301	13.996
14	41.739	-71.889	68.0476	68.0476	0.22	14.466
15	41.751	-71.889	70.7569	72.1	0.224	14.181
16	41.743	-71.902	66.3741	65.2	3.001	16.271
17	41.751	-71.889	72.1251	72.1	0.289	14.181
18	41.77	-71.871	121.3284	121.3284	-11.889	10.051
19	41.765	-71.869	145.9669	148.2	-17.441	10.265
20	41.76	-71.868	146.6369	146.6369	-17.291	10.551
21	41.754	-71.868	164.6692	158.2	-19.951	10.656
22	41.75	-71.868	161.6431	161.6431	-21.032	10.63
23	41.745	-71.869	137.7311	132.7	-15.331	11.083
24	41.74	-71.872	130.1416	127.3	-14.416	11.361
25	41.735	-71.877	97.7004	95.8	-8.412	11.581
26	41.737	-71.886	73.0886	70.5	-1.262	13.597
27	41.74	-71.883	75.1451	74.2	-2.404	12.914
28	41.734	-71.891	71.8709	71.8709	-1.016	14.398
29	41.74	-71.895	73.4486	73.4486	0.109	15.282
30	41.742	-71.9	63.8405	65.3	2.42	15.798
31	41.751	-71.889	72.1505	72.1	0.282	14.184
32	41.775	-71.883	82.758	82.758	-3.732	10.158

33	41.78	-71.882	89.338	86.4	-4.288	9.8308
34	41.786	-71.879	84.5894	89.4	-4.865	9.3959
35	41.791	-71.88	70.2669	75.3	-1.918	9.1005
36	41.797	-71.88	76.3687	80.8	-2.497	9.0514
37	41.803	-71.88	76.6066	79.6	-1.853	8.9663
38	41.808	-71.88	69.9951	74.1	-0.474	8.7631
39	41.738	-71.904	66.9443	72	1.575	16.701
40	41.733	-71.903	61.8844	67	1.651	16.257
41	41.742	-71.907	69.6036	71.8	2.401	17.103
42	41.751	-71.889	67.6007	72.1	0.145	14.185
43	41.747	-71.907	80.5309	83.4	0.131	16.709
44	41.751	-71.903	78.49	78.49	0.944	16.19
45	41.757	-71.9	73.4847	73.4847	1.755	15.489
46	41.762	-71.9	55.059	58.8	4.536	14.921
47	41.767	-71.9	54.6623	57.7	4.285	14.01
48	41.772	-71.897	76.4233	74.2	0.639	13.254
49	41.776	-71.895	72.0645	74.4	0.06	12.347
50	41.78	-71.892	69.3836	71.9	-0.245	11.146
51	41.785	-71.887	61.9165	62.5	0.183	9.3504
52	41.789	-71.885	55.9355	58.2	1.09	9.0402
53	41.795	-71.884	53.8357	53.8357	2.923	9.4758
54	41.8	-71.885	67.7559	63.9	1.292	9.3721
55	41.751	-71.889	70.2604	72.1	0.125	14.183
56	41.772	-71.937	68.7818	69.6	7.132	18.746
57	41.768	-71.939	62.7736	61.9	8.045	18.519
58	41.765	-71.937	62.6701	63.3	7.912	18.961
59	41.76	-71.934	72.1211	72.1211	4.899	18.103
60	41.757	-71.931	77.8921	77.8921	3.515	18.16
61	41.753	-71.928	81.1162	79	3.28	18.498
62	41.75	-71.924	74.4579	81.4	2.975	18.957
63	41.749	-71.917	45.4832	48.6	8.521	18.156
64	41.745	-71.921	67.2883	69.5	4.81	18.867
65	41.742	-71.926	63.2079	66.7	5.373	19.133
66	41.74	-71.931	65.4118	63.9	6.025	19.455
67	41.739	-71.937	59.971	58.6	7.545	19.967
68	41.772	-71.937	65.2943	69.6	7.146	18.747
69	41.769	-71.942	61.1839	61.1839	7.378	17.564
70	41.765	-71.944	66.1742	61.3	7.43	17.993
71	41.762	-71.947	61.9625	61.9625	6.579	17.552
72	41.757	-71.951	44.9814	45.5	10.028	18.134
73	41.755	-71.947	51.3424	49.4	9.466	18.544
74	41.759	-71.945	55.1808	56.4	8.572	18.679
75	41.759	-71.939	59.9661	62.5	7.119	18.369

76	41.759	-71.925	64.9272	64.9272	5.614	17.363
77	41.763	-71.922	86.2309	84	1.841	16.947
78	41.769	-71.921	99.8243	100.4	-1.373	16.472
79	41.772	-71.937	65.6995	69.6	7.332	18.745
80	41.773	-71.931	80.3498	82	4.191	18.01
81	41.774	-71.923	89.4792	88.7	1.648	16.742
82	41.779	-71.922	102.2527	99.3	-0.425	16.3
83	41.785	-71.921	91.295	96.3	0.323	15.947
84	41.788	-71.919	69.5226	71.8	4.777	15.267
85	41.792	-71.915	82.3861	78.9	3.253	14.81
86	41.796	-71.91	71.0504	71.0504	4.098	13.801
87	41.772	-71.937	65.0704	69.6	7.289	18.748
88	41.772	-71.937	68.9796	69.6	7.061	18.747
89	41.778	-71.936	92.3796	92.3796	1.903	17.55
90	41.782	-71.936	100.0014	100.0014	-0.063	16.698
91	41.788	-71.933	123.4919	116.7	-4.113	15.446
92	41.792	-71.932	116.3149	116.3149	-4.565	14.516
93	41.795	-71.928	93.7989	93.2	0.214	14.502
94	41.799	-71.926	105.826	103	-2.094	13.749
95	41.803	-71.924	102.7087	102.7087	-3.308	12.131
96	41.809	-71.924	94.7872	89	-0.991	11.286
97	41.8	-71.93	82.0866	82.0866	1.37	12.993
98	41.801	-71.936	86.448	88.8	0.238	13.153
99	41.798	-71.939	103.2844	104.9	-2.742	13.612
100	41.793	-71.943	80.0637	80.0637	2.048	13.924
101	41.792	-71.937	88.1269	88.6	0.597	14.197
102	41.772	-71.937	65.3433	69.6	7.077	18.748
103	41.791	-71.924	83.318	84.7	2.9	15.739
104	41.788	-71.913	77.6043	72.7	3.637	14.427
105	41.787	-71.907	77.6303	68.3	3.739	13.683
106	41.787	-71.901	70.7457	69.5	2.605	12.765
107	41.788	-71.895	68.2022	70	1.224	11.413
108	41.792	-71.894	64.3079	66.4	1.785	10.86
109	41.798	-71.894	67.5905	66.9	2.157	10.736
110	41.801	-71.899	71.2166	71.8	3.038	12.339
111	41.804	-71.902	63.6599	63.6599	5.175	12.507
112	41.808	-71.905	85.7228	84.5	2.268	13.276
113	41.772	-71.937	68.9196	69.6	7.565	18.747